Nanoscale

Printing rare-earth-free (REF) magnetic inks: synthesis, formulation, and device applications

Journal:	*Nanoscale*
Manuscript ID	NR-REV-10-2024-004035.R1
Article Type:	Review Article
Date Submitted by the Author:	06-Dec-2024
Complete List of Authors:	Moni, Hur-E-Jannat ; Texas Tech University, Chemical Engineering Rezaei, Bahareh; Texas Tech University, Electrical and Computer Engineering Karampelas, Ioannis H.; Nemak USA, Inc. Saeidi, Mortaza ; California State University Long Beach, Gomez-Pastora, Jenifer; Texas Tech University, Chemical Engineering Wu, Kai; Texas Tech University, Electrical and Computer Engineering; Zeng, Minxiang; Texas Tech University, Chemical Engineering

Printing rare-earth-free (REF) magnetic inks: synthesis, formulation, and device applications

Hur-E-Jannat Moni[1,#], Bahareh Rezaei[2,#], Ioannis H. Karampelas[3], Mortaza Saeidi-Javash[4], Jenifer Gómez-Pastora[1], Kai Wu[2], Minxiang Zeng[1,*].

[1]Department of Chemical Engineering, Texas Tech University, Lubbock, TX 79409, United States.
[2]Department of Electrical and Computer Engineering, Texas Tech University, Lubbock, TX 79409, United States.
[3]Nemak USA, Inc., 3101 S Taylor Dr, Sheboygan, WI 53081, United States.
[4]Department of Mechanical and Aerospace Engineering, California State University Long Beach, Long Beach, California, United States.
[#]The authors contribute equally to this manuscript.

Abstract

Additive manufacturing (AM) of magnetic materials has recently attracted increasing interest for various applications but is often limited by the high cost and supply chain risks of rare-earth-element (REE) magnetic precursors. Recent advances in nanomanufacturing have enabled the development of rare-earth-free (REF) magnetic materials, such as spinel ferrites, hexaferrites, MnAl, MnBi, Alnico, FePt, and iron oxides/nitrides, which offer promising alternatives for printing high-performance magnetic devices. This review provides a detailed overview of the latest developments in REF magnetic materials, covering both synthesis strategies of REF magnetic materials/nanomaterials and their integration into AM processes. We summarize the design and formulation of magnetic inks, emphasizing the unique properties of REF ferromagnetic and ferrimagnetic systems and their adaptability to AM techniques like direct ink writing, inkjet printing, aerosol jet printing, and screen printing. Key advancements in materials chemistry, ink rheology, and device performance are discussed, highlighting how the structure of REF magnetic materials impacts device functionalities. This review concludes with a perspective on the pressing challenges and emerging opportunities in AM of REF magnetic inks. Through this review, we aim to offer insights in the structure-processing-property relationship of REF magnetic inks and guide the design of next-generation printable magnetic systems in a scalable, cost-effective, and sustainable manner.

1. Introduction

Magnetic materials, particularly ferromagnetic and ferrimagnetic materials, are crucial for a diverse range of technological applications, including energy conversion,[1-4] data storage,[5] and biomedical uses.[6-8] Rare earth elements (REE) are often added to ferromagnetic materials to improve their performance; for example, neodymium (Nd) is incorporated in permanent magnets to create high strength magnetic field sources used in electric vehicles and wind turbines.[9] These REE materials enhance the magnetic strength and thermal stability of ferromagnetic materials, allowing for smaller and more efficient designs. In 2014, the annual production of Nd-Fe-B magnets was estimated at 79,500 tons, with 69.4% of the total Nd production allocated to permanent magnet manufacturing.[10] However, the dependency on REEs brings challenges such as environmental pollution from mining processes, geopolitical risks from concentrated supply chains, and

price volatility.[11] Consequently, the development of rare-earth-free (REF) systems with high performance is urgently needed.

From a manufacturing perspective, permanent magnets are primarily fabricated using methods like sintering, injection molding, and compression bonding.[11-13] These methods, despite being effective, often suffer from limited design freedom and excessive material waste. To address these drawbacks, additive manufacturing has become an emerging approach to fabricate magnetic materials with complex geometries and to allow multi-function integration. Magnetic particles/nanoparticles, a key building block in magnetic inks for additive manufacturing, enable the creation of bulk magnetic materials with tunable magnetic properties. To date, a number of printing methods have been used to manufacture magnetic materials, including ink-based printing (e.g., extrusion printing,[5, 14, 15] inkjet printing,[16, 17] screen printing,[1] binder jet printing,[18] etc.) and ink-free printing (e.g., stereolithography,[19, 20] direct energy deposition,[21, 22] powder bed fusion,[23, 24] etc.), where ink-based printing will be the primary focus for this review due to the easy integration with magnetic nanoparticles. For example, direct ink writing (DIW) printing allows for the fabrication of flexible magnetic sensors[25-27] and energy harvesters[5] by integrating magnetic particles into a polymer matrix, significantly expanding the application space of magnetic technologies with increased efficiency and design flexibility. Leveraging the design freedom of additive manufacturing, complex structures such as patterned, anisotropic, and magnetic soft actuators have been demonstrated.[26, 28-37]

Despite recent advancements in printing REF magnetic devices, a thorough understanding of the interplay between materials chemistry, processing strategies, and device designs is still lacking, especially at the ink level. This review proposes a bottom-up approach to explore the core relationships between magnetic material synthesis, ink formulation, printing processes, and device applications. In **Section 2**, we begin with an overview of REF magnetic materials with a particular focus on permanent magnet materials due to their excellent coercivity, remanence, and magnetic energy product. This section also showcases different synthesis methods for REF magnetic particles/nanoparticles, which are nanoscale building blocks for printing bulk magnetic materials and devices. We then discuss the latest advances in magnetic ink chemistry in **Section 3**, including ink formulation and design principles. Following this, we introduce various printing methods that leverage functional magnetic inks and summarize recent advancements in post-processing approaches. In **Section 4**, our discussion extends beyond permanent magnet applications and explores cutting-edge domains such as magnetic sensors and energy conversion devices. Lastly, in **Section 5**, this review is concluded by highlighting promising directions and research opportunities for printing-related magnetic technologies, along with the challenges faced in mass commercialization. This review aims to summarize the emerging materials processing and device manufacturing techniques, to elucidate the processing-structure-property relationships of printed materials and systems, and to drive the rapid development of this interdisciplinary research field, which spans from the design of nanoscale building blocks to the manufacturing of macroscopic devices. It is important to note that this work focuses primarily on electronics-related magnetic materials and devices, while topics like magnetic calorimetric cells[38-41] and magnetophoresis-based devices[42, 43] are beyond its scope and can be found in other recent reviews.

2. Rare-earth-free magnetic materials and synthesis method

2.1. Overview of different REF magnetic systems

Magnetic materials are crucial in critical technologies like electronics, high-energy product motors, transformers and generators, data storage systems, magnetic levitation transportation systems, electric

vehicles, wind turbines, and medical devices including heart pumps and magnetic resonance imaging (MRI) machines.[44, 45] REEs such as Nd, Sm, Dy, Pr, and La, are often added to magnetic materials (particularly permanent magnets) to optimize their magnetic properties.[46] Nevertheless, controlling the cost and environmental impact of REE-based magnet production poses a major challenge as the demand for permanent magnets keeps rising. Moreover, questions about these REEs' availability, extraction challenges, environmental pollution, and potential effects on national security have been brought up by their strategic and unstable origins. The increasing price of rare-earth metals further worsens the current situation of this sector,[47] and as a result, there has been a noticeable change in the magnetic materials community toward the creation of novel, alternative magnetic materials made entirely from REF elements.[45, 46] These REF magnetic materials show great potential as permanent magnets due to their high magneto-crystalline anisotropy and energy product.[46] In this section, we mainly focus on REF materials for magnet applications, where a general overview of magnetic materials has been reviewed elsewhere.[11, 48] A high-performing magnetic substance should fulfill multiple essential requirements. Firstly, a high saturation magnetization (M_S), high uniaxial magnetic anisotropy constant (K), and high Curie temperature (T_C) should all be present in the magnet's main phase. Secondly, the material needs to have a particular micro- or nanostructure that makes it possible to transform its intrinsic qualities into extrinsic qualities that are technically appropriate. Key extrinsic characteristics are a high remanent magnetization (M_r), which is dictated by M_S, texture degree, and minimal secondary phases, and coercivity (H_C), which is mainly affected by K, grain size, and the designed intergranular phase.[49] While this section does not intend to cover all types of magnetic materials, **Figure 1** shows several prominent examples of REF ferromagnetic and ferrimagnetic materials.

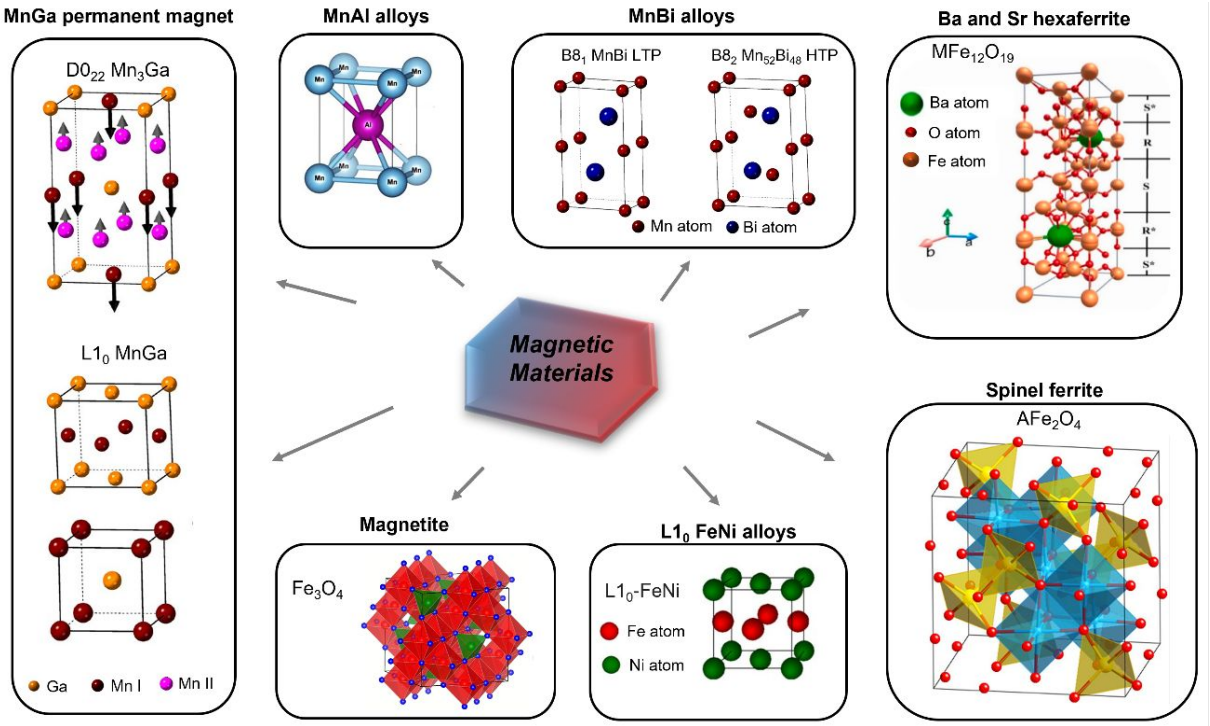

Figure 1. Examples of various REF magnetic materials.[50-56] Reproduced from ref. 50 with permission from Elsevier, copyright 2022. Reproduced from ref. 51 with permission from Springer Nature, copyright 2016. Reproduced from ref. 52 with permission from Springer Nature, copyright 2017. Reproduced from ref. 53 with permission from Elsevier, copyright 2022. Reproduced from ref. 54 with permission from Elsevier,

copyright 2020. Reproduced from ref. 55 with permission from Elsevier, copyright 2021. Reproduced from ref. 56 with permission from American Physical Society, copyright 2021.

2.1.1. Spinel ferrite

Depending on their original crystal lattice, ferrites have different structural properties from garnet, hexagonal, and spinel. A spinel crystal structure is generally represented by the chemical formula AB_2O_4. In this instance, A and B stand for distinct metal cations that are located inside the crystal in tetrahedral (A site) and octahedral (B site) locations. The usual formula for spinel ferrites is MFe_2O_4, where M represents a divalent metal ion, and Fe is in the +3 state.[57] The specific type, concentrations, and locations of metal cations including Ni, Mn, Mg, Co, Li, and Cu, have a major impact on the physicochemical characteristics of ferrites. A single unit cell has 64 tetrahedral and 32 octahedral sites; however, only 8 and 24 sites are occupied by cations. Based on the distribution of cations in the octahedral and tetrahedral positions, spinel ferrites are classified into normal, inverse, and mixed spinel categories.[58] $ZnFe_2O_4$ is a typical example of a normal spinel, with Fe^{3+} ions found in the octahedral positions and Zn^{2+} ions in the tetrahedral sites.[59] $NiFe_2O_4$ is an example of the inverse spinel category, with half of the Fe^{3+} ions and Ni^{2+} ions located in the octahedral sites and the other half of the Fe^{3+} ions in the tetrahedral sites.[60] This suggests that the magnetic characteristics of spinel ferrites may be affected by the distribution of cations between these two interstitial sites.[61, 62] Also, in spinel ferrites, oxygen ions control magnetic interactions between metal cations at different sites, leading to ferrimagnetism. The magnetic properties of spinel ferrites depend on their composition, dopants, and synthesis conditions, influencing characteristics like magnetic saturation and coercivity.[61]

2.1.2. Hexaferrite

Hexaferrites are ferrites with a hexagonal crystal structure, classified into six types based on their structures: M-type ($BaFe_{12}O_{19}$), Y-type ($Ba_2M_2Fe_{12}O_{22}$), W-type ($BaM_2Fe_{16}O_{27}$), Z-type ($Ba_3M_2Fe_{24}O_{41}$), X-type ($Ba_2M_2Fe_{28}O_{46}$), and U-type ($Ba_4M_2Fe_{36}O_{60}$).[63] M-type hexaferrites have a space group of p63/mmc and a magnetoplumbite configuration.[64] Barium hexaferrite (BHF), also known as $BaO{\cdot}6Fe_2O_3$ or $BaFe_{12}O_{19}$, is an M-type hexaferrite.[55] The Ba^{2+} ion's large size causes a little lattice disruption around it, which allows it to exhibit considerable magnetic uniaxial anisotropy. The magnetic easy axis is the crystallographic c-axis. Because of its similarity with the magnetoplumbite crystal structure, BHF has high magneto-crystalline anisotropy, high M_S, high T_C, and substantial H_C, making it stable and suitable for a wide range of uses. Doping, calcination, and sophisticated synthesis techniques can be used to improve these characteristics.[65] The BHF crystal structure is described as RSR*S*, where each (*) denotes a block that has been rotated 180 degrees along the hexagonal's c-axis (**Figure 1 top right**). The M-type hexaferrite is depicted as an S block with cubic packing and an R block with hexagonal packing. The shape, surface area, stability, and purity of ferrite materials are all impacted by the synthesis process and these parameters need to be carefully designed as they are essential for producing high-quality materials. The size and distribution of iron ions, the strength of the iron-oxygen interactions, and the presence of other ions (like Ba) in the

crystal structure are some of the variables that affect the BHF's magnetic properties.[66-68] By adjusting these variables, the magnetic properties of $BaFe_{12}O_{19}$ may be modified, which makes it useful for a variety of applications like microwave absorption and permanent magnets.[65]

2.1.3. $L1_0$ FePt and FeNi alloys

Iron is one of the most promising candidates among REF elements due to its abundance and high Ms. Iron-based magnets, including FePd, FePt, FeCo, $Fe_{12}N_2$, FeNi, and Fe_3Se_4, have a rich history of applications, such as the use of ferrites in navigation dating back to ancient times. Several iron-based compounds with significant H_C and large Ms have shown potential for different applications, including green energy applications.[69] $L1_0$-ordered materials, including FePt, FePd, CoPt, FeNi, and similar compounds, have shown great promise as replacements for rare-earth-based permanent magnets. Because of their tetragonal lattice structure and the monoatomic ordering of unlike atomic pairs along the easy magnetization axis, these materials show strong magneto-crystalline anisotropy. Over the years, magnetic compounds crystallizing in the $L1_0$-ordered structure have attracted a lot of attention due to their industrial uses as well as their fundamental magnetic properties.[70] It is commonly known that the binary FePt alloys exhibit considerable magnetic anisotropy in the ordered $L1_0$ phase. The high magnetocrystalline anisotropy constant of 7×10^6 J/m^3 in $L1_0$-ordered, face-centered cubic (FCC) FePt nanocrystals is very attractive since it guarantees the magnetic stability of small particles down to 2-3 nm at ambient temperature.[51] FePt nanocrystals have considerable ferromagnetism and may stabilize at room temperature, which makes them a desirable option for a variety of technological advancements.[48] Additionally, the chemical structure in $L1_0$-FeNi alloy makes it a promising candidate for the next generation of REF permanent magnets due to its high Ms and T_C.[71, 72] As $L1_0$-FeNi is made up of common elements like Fe and Ni, it has a remarkable uniaxial magnetic anisotropy of $>1 \times 10^6$ J/m^3. Similar to Nd-Fe-B, $L1_0$-FeNi has a saturation magnetic flux density of 1.6 T ($154\ Am^2/kg$). The Curie point of this material is 550 °C or higher. $L1_0$-FeNi is an ordered alloy with an equiatomic Fe and Ni content. The atomic layers of Fe and Ni are stacked alternately along the c-axis (easy axis)of the FCC crystal structure.[52]

2.1.4. Metastable phase α"-$Fe_{16}N_2$

Since Jack *et al.* reported the metastable phase α"-$Fe_{16}N_2$ in 1951, its magnetic properties have shown potential for applications in speakers, hard drives, motors, wind turbines, smartphones, audio devices, and power generation machines.[73] A quick quenching technique from γ-Fe-N-austenite has been successfully used to produce the powder samples of α"-$Fe_{16}N_2$, an important step in the creation of this special phase. According to the iron nitride phase diagram, the (FCC) Fe phase predominates at high temperatures above 590 °C, and random occupation of octahedral interstices made possible by the insertion of nitrogen (N) atoms into the structure leads to the γ-Fe-N phase throughout a broad range of nitrogen concentrations. The potential of α"-$Fe_{16}N_2$ to replace or enhance conventional REE-based magnets makes its production and optimization still of interest. Researchers can modify the magnetic characteristics of α"-$Fe_{16}N_2$ to suit particular applications by comprehending the behavior of iron and nitrogen at different temperatures and concentrations. N atoms are added during the nitriding step, allowing for random occupation in the octahedral sites and the formation of the γ-Fe-N phase over a broad N concentration.[73-75] Refinement of the synthesis process and investigation of the stability and scalability of α"-$Fe_{16}N_2$ could result in more

sustainable magnetic materials. For example, the austenite phase (γ-phase) is dominant at temperatures above 650 °C, whereas the martensite phase remains stable below 214 °C.[76]

2.1.5. MnAl alloys

Bulk Mn is antiferromagnetic, but it can become a potent ferromagnet when combined with other elements. Mn-Bi and Mn-Al alloys have the potential to be gap magnets (i.e., filling the gap between the powerful Nd magnets and the weaker ferrite magnets), even though several Mn-based systems, such as Mn-B, Mn-Ga, Mn-Ge, Mn-As and Mn-Sb, exhibit ferromagnetism.[11] In MnAl alloys, the metastable ferromagnetic body-centered tetragonal (BCT) τ phase is the primary source of the magnetic characteristics. The τ phase of MnAl has attracted interest as a notable REF magnetic material because of a number of beneficial properties.[77] An annealed ε phase or a controlled cooling from the high-temperature equilibrium hexagonal ε phase are the two ways to reach this τ phase within a restricted composition range.[78, 79] It offers exceptional corrosion resistance, high strength, and high elastic modulus, along with excellent machinability and relatively low-cost constituent elements. Consequently, MnAl is beginning to show promise as a substitute for traditional, high-strength REE magnets, especially in the fields of alternative energy and hybrid devices.[78] However, MnAl suffers from lower magnetization below 473 K and instability of its ferromagnetic τ-phase, making it challenging to improve its performance without the addition of a third element.[44, 50, 77, 80]

2.1.6. MnBi alloys

Another promising REF substitute for Nd-based permanent magnets is Mn-Bi alloys. The combination of readily achievable magnetic hardness and a remarkable positive temperature coefficient of H_C, along with the low cost of raw materials and high magnetocrystalline anisotropy (1.6×10^6 J/m^3) at room temperature[81] has attracted attention worldwide for the development of MnBi magnets with a sufficiently high magnetic energy density, despite concerns regarding their susceptibility to oxidation and the affordability of raw Bi in the event of increased demand.[82-84] There are two MnBi phases, namely, (1) α-MnBi, also known as low-temperature phase (LTP) MnBi, with the chemical formula MnBi, and (2) β-MnBi, also referred to as the high-temperature phase (HTP) MnBi, with the chemical formula $Mn_{1.08}Bi$. The β-MnBi phase is formed at 446 °C from the Mn + Liquid-Bi mixture, while the α-MnBi phase is formed at 355 °C from the β-MnBi + Liquid-Bi mixture. The LTP MnBi is highly stable and ideal for energy applications such as permanent magnet motors, even at high temperatures up to about 628 K, due to its positive temperature coefficient of H_C, which increases its magnetic strength with rising temperature.[76, 81] On the other hand, the HTP quickly switches back to the LTP at around 440 K. This behavior makes HTP promising for use in data storage and magneto-optics.[53, 85]

2.1.7. MnGa permanent magnet

The MnGa binary system creates a variety of intermetallic compounds. Some of these phases show magnetic characteristics. As shown in **Figure 1**, two crystal structures are highlighted particularly for permanent magnet applications: the ferrimagnetic tetragonal $D0_{22}$ phase and the ferromagnetic tetragonal $L1_0$ phase.[53, 86] In general, the $D0_{22}$ phase occurs in the Mn_3Ga region of the phase diagram, whereas the $L1_0$ phase is linked with the nearly equiatomic fraction region, MnGa. Nevertheless, the precise phase

boundaries for MnGa materials remain a matter of debate. One interesting feature of these compounds is their capacity to modify elemental compositions to suit certain applications, thus customizing magnetic characteristics.[87, 88] The lattice parameters of the ferrimagnetic $D0_{22}$ unit cell are a = 0.391 nm and c = 0.710–0.717 nm, where the c value increases with increasing Ga concentration. Two different types of Mn atoms, Mn_I and Mn_{II}, with opposing magnetization orientations and magnetic moments of -2.8 μ_B and 1.6 μ_B, respectively, are found within the unit cell, where μ_B is Bohr magneton. With a density of 7180 kg/m^3, the theoretical maximum energy product $(BH)_{max}$ is approximately 143 kJ/m^3, the uniaxial magneto-crystalline anisotropy energy is around 1 MJ/m^3. The MnGa intermetallic compounds have potential uses in many different fields. Magnetic tunnel junctions (MTJs) and exchange-biased spin valves (EBSVs) are two examples of spintronic devices that utilize the large exchange-bias field in $D0_{19}$-type Mn_3Ga coupled with a ferromagnetic material.[89, 90] High T_C, H_C, spin polarization, and magnetic anisotropy are characteristics of ferromagnetic $D0_{22}$-type Mn_3Ga and ferromagnetic $L1_0$-type MnGa, which make them attractive materials for spintronic devices and REF hard magnets.[91]

2.1.8. Alnico magnet systems

Al-Ni-Co permanent magnets or Alnico magnets are well-known for having high Curie points up to 850 °C, which enable them to be used in high-temperature applications in place of other magnet types.[92] Commercial grades of these magnets range from Alnico-1 to Alnico-9, with each grade being identified by the alloy composition and production parameters. Alnico-5 through Alnico-9 are the most well-known alloys in these series; to improve their magnetic properties, they are either heat-treated in a magnetic field or grain-aligned.[92] Alnico has been widely utilized in high-temperature devices because of the exceptional Ms and extraordinary thermal stability, which can result in cheaper manufacturing costs for specific high-temperature applications. Iron, nickel, cobalt, and aluminum coexist in Alnico alloys at temperatures higher than 1200-1250 °C.[93] When the molten alloy cools below 1200-1250 °C, the system separates into two phases: a ferromagnetic Fe-Co phase and a paramagnetic Al-Ni phase. Key elements that impact Alnico magnets' performance include their composition, shape, distribution, and phase.[94, 95] **Table 1** provides an overview of the magnetic characteristics of different grades of cast Alnico magnets.

Table.1. Magnetic properties of some representative cast Alnico alloys.[96] B_r: remanent magnetization, is the magnetic flux density retained by a magnetic material when the external magnetizing field is removed; H_C: coercivity, is the intensity of the external magnetic field required to reduce the magnetization of a magnetic material to zero after it has been magnetized to saturation; $(BH)_{max}$: maximum energy product, is the highest product of the magnetic flux density and the magnetic field strength that a material can achieve, indicating its maximum energy density; T_C: Curie temperature, is the temperature above which a ferromagnetic or ferrimagnetic material loses its permanent magnetism. Adapted with permission from Ref. 83 at OCP Publishing.

Approximate composition of alloy (balance Fe for all alloys)	B_r (T)	H_C (kA/m)	$(BH)_{max}$ (kJ/m³)	T_C (°C)
Co (5%) Ni (20%) Al (12%)	0.71	38	11.1	760
Co (13%) Ni (17 -19%) Al (10%) Cu (3-6%)	0.71-0.78	46	13.5	800-815

Ni (25%) Al (12%) Cu (0-3%)	0.63-0.70	45	10.7	740-760
Co (5%) Ni (27-28%) Al (12%)	0.52-0.55	57	11.1	760
Co (24%) Ni (14%) Al (8%) Cu (3%)	1.28	51	43.8	890
Co (24%) Ni (14%) Al (8%) Cu (3%)	1.28-1.33	53	57.7	860
Co (24%) Ni (14%) Al (8%) Cu (3%)	1.35	59	59.7	890
Co (24%) Ni (16%) Al (8%) Cu (3%) Ti (1%)	1.05	62	31.0	860
Co (35%) Ni (15%) Al (7%) Cu (4%) Ti (5%)	0.82	148	42.2	860
Co (35%) Ni (15%) Al (7%) Cu (4%) Ti (5%)	1.06	119	71.6-73.6	860
Co (25%) Ni (13%) Al (8%) Cu (3%) Nb (1%)	1.35	59	60-69	860

2.2. Synthesis methods for REF magnetic materials/nanomaterials

The synthesis of REF magnetic materials/nanomaterials has been an area of significant study in recent decades, particularly to produce stable, monodisperse, shape-controlled particles. In recent years, numerous publications have highlighted effective synthesis methods for creating high-quality magnetic particles across different length scales.[97] Several techniques can be employed to synthesize these particles, including co-precipitation, microemulsion, hydrothermal, thermal decomposition, ball milling, and laser ablation methods.[98] These methods offer different advantages and can lead to the production of particles with specific size, shape, and stability characteristics. Rather than providing an exhaustive overview of all available synthesis methods and their variations, in this section, we focus on discussing each synthetic pathway. It is worth noting that not all examples presented in the following subsections are printed magnetic materials. Instead, these magnetic materials have the potential to be formulated in magnetic inks for additive manufacturing.

2.2.1. Co-precipitation

Co-precipitation is a versatile and widely used method for synthesizing diverse materials, particularly in the production of fine nanopowders with uniform composition. The method involves the precipitation of desired materials from a solution containing metal salts or other precursors using a precipitant (e.g., pH modification) either at room temperature or at a higher temperature.[97] The final product is obtained by calcining the precipitates that are produced. The production of high-quality particles using co-precipitation is often scalable, but it necessitates careful control over several variables, including temperature, mixing time, reactant concentration, ligands, and pH.[99] By controlling these factors, co-precipitation can produce high-quality magnetic materials with tailored properties.

For example, in Kurichenko *et al.* study, they reported a FeNi $L1_0$ phase in chemically co-precipitated FeNi particles through a thermal treatment procedure that involves cycling oxidation and reduction processes at 320 °C (**Figure 2A**). The successful formation of the tetrataenite phase in the samples was validated by Differential Scanning Calorimetric (DSC) analysis and magnetic property characterizations. **Figure 2B**

displays the DSC curves obtained during the heating (solid line) and cooling (dashed line) of the samples. All samples exhibit consistent behavior in the heat flow versus temperature dependence, showing distinct anomalies at 480 °C and 730 °C. The assessed anisotropy field of 18 kOe (=1.43×10^6 A/m) agreed with the FeNi $L1_0$ phase experimental data (**Figure 2C**). The researchers suggested modifying the shape of the particles into anisotropic forms, such as nanorods or nanotubes, to enhance the anisotropy field, which is essential for permanent magnet applications.[98]

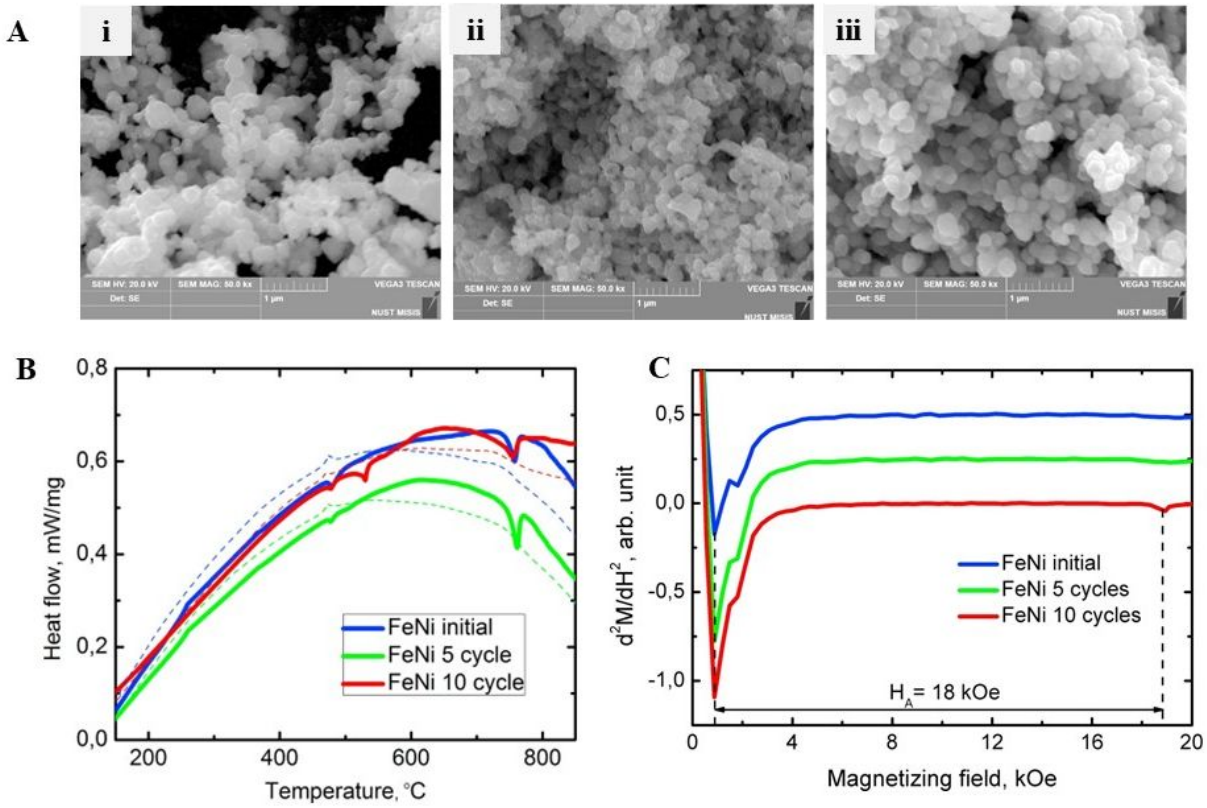

Figure 2. (A) SEM images of FeNi nanoparticles: (i) initial sample, (ii) after 5 treatment cycles, and (iii) after 10 treatment cycles. (B) DSC curves of initial FeNi samples and the samples subjected to 5 and 10 treatment cycles upon heating (solid lines) and cooling (dashed lines). (C) Singular Point Detection (SPD) curves of initial FeNi samples and the samples subjected to 5 and 10 treatment cycles.[98] Reproduced from ref. 98 with permission from Elsevier, copyright 2019.

2.2.2. Microemulsion

The microemulsion synthesis method can be used to produce magnetic nanomaterials, offering advantages such as fine control over particle size and uniformity, which can impact the magnetic properties of the final product. Microemulsions are stable mixtures of oil and water in the presence of surfactants, and sometimes, a cosurfactant. Amphiphilic surfactants, with their hydrophobic tails dissolved in the oil phase and their hydrophilic head groups in the watery phase, produce a monolayer at the microemulsion interface.[100] Typically, the self-assembled structures lead to the creation of spherical micelles with nanometer-scale dimensions. As seen in **Figures 3A** and **3B,** typical microemulsions include water-in-oil (w/o) or direct oil-

in-water (o/w) systems. The method allows for the synthesis of particles in a controlled, confined environment, leading to uniform particle size distributions.[101] **Figure 3C** shows some common examples of surfactants.

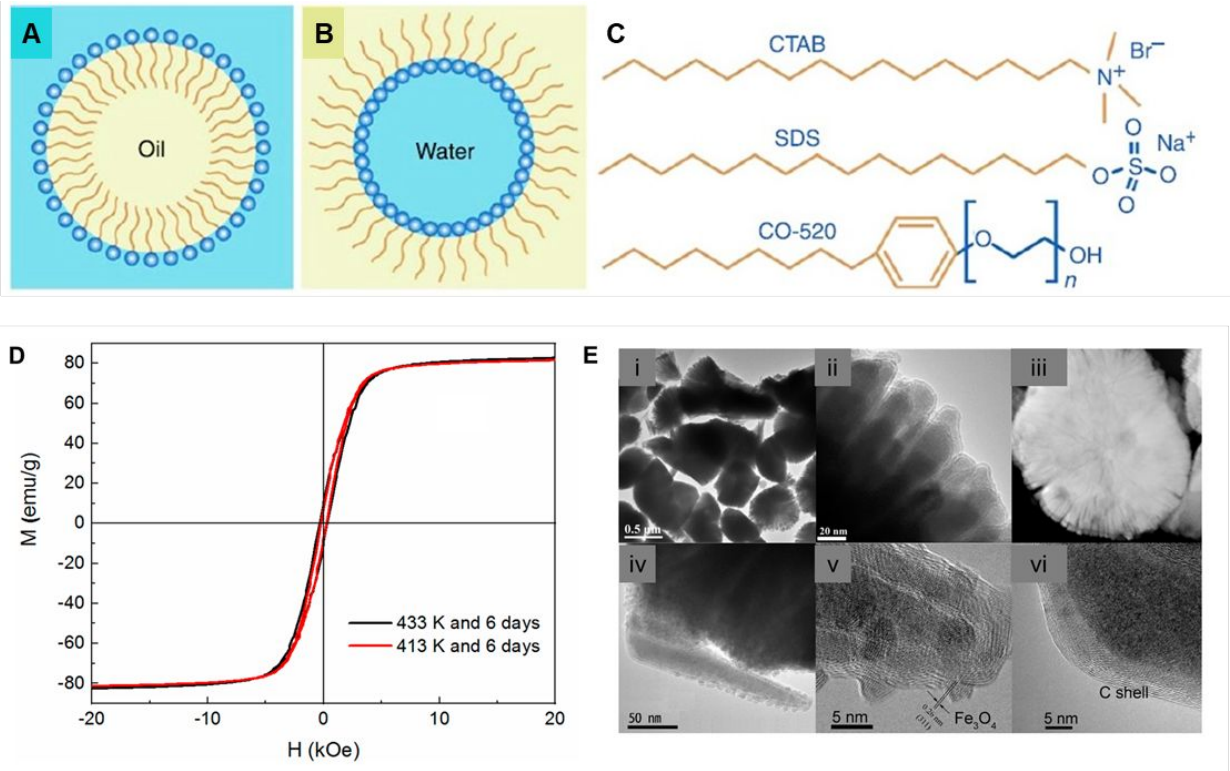

Figure 3. Schematic illustration of (A) oil in water emulsion and (B) water in oil emulsion. (C) Common surfactants include CTAB (cetyltrimethylammonium bromide), SDS (sodium dodecyl sulfate), and IGEPAL CO-520 (polyoxyethylene (5) nonylphenylether).[101] (D) Magnetic hysteresis loops of the α″-$Fe_{16}N_2$ at C nanocones synthesized at 433 K for six days and at 413 K for six days, respectively. (E)(i,ii) TEM images and (iii) HADDF (High-Angle Annular Dark-Field) image of α″-$Fe_{16}N_2$ nanocones synthesized at 433 K for six days. (iv) TEM image for a separate α″-$Fe_{16}N_2$ nanocone and its corresponding HRTEM image for (v) Fe_3O_4 nanocrystals on the surface of the thinner end and (vi) carbon shell of the thicker end.[102] (A-C) Reproduced from ref. 101 with permission from Elsevier, copyright 2011. (D-E) Reproduced from ref. 102 with permission from MDPI, copyright 2021.

Li *et al.* synthesized carbon-coated tetragonal α″-$Fe_{16}N_2$ nanocones using a single-pot microemulsion method, where tetraethylenepentamine (TEPA) served as the N/C source and $Fe(CO)_5$ as the iron source.[102] The significant magnetocrystalline anisotropy energy of α″-$Fe_{16}N_2$ nanocrystals was responsible for the anisotropic growth of the tetragonal α″-$Fe_{16}N_2$. The non-zero magnetization caused the carbon-coated α″-$Fe_{16}N_2$ to aggregate and form a fan-shaped microstructure (**Figure 3E**). The powder XRD pattern reveals that Fe_3O_4 and α-Fe were the predominant phases in the sample synthesized over three days at 393 K. After a three-day nitridation process at 403 K, the powder XRD shows the peaks of α-Fe (JCPDS card 06−696) and α″-$Fe_{16}N_2$ (JCPDS card 78−1865), along with a small amount of Fe_3O_4, as evidenced by the weak (311) peak at $2\theta = 35.4°$. Also, the primary phase α-$Fe_{16}N_2$ and a trace amount of Fe_3O_4 were present in the

powder by increasing the reaction temperature and duration to 433 K and six days. At room temperature, their H_c and Ms were 320 Oe (=25.5 kA/m) and 82.6 emu/g (=82.6 A·m²/kg), respectively (**Figure 3D**).

2.2.3. Hydrothermal

The hydrothermal approach involves the conversion of specific salt solutions at elevated temperatures.[62, 103] The process of growing crystals from solutions has drawn a lot of interest in a range of material compositions and morphologies since it is straightforward and inexpensive. The benefit of hydrothermal growth over solvothermal techniques is that it can be carried out in a safe and eco-friendly environment (employing aqueous solution instead of organic solvents).[104] High temperature and high pressure equipment are required for the hydrothermal process, which can yield uniformly dispersed particles with relatively narrow particle size distributions, good crystallinity, and controllable morphologies.[99] Sun *et al.* hydrothermally synthesized MnBi particles with an H_C of 8 kOe (=6.37×10^5 A/m) at 5 K and an M_S of 2.37 emu/g (=2.37 A·m²/kg).[105] This aqueous solution-based method provided a flexible, scalable approach to the production of MnBi@Bi by eliminating the requirement of harsh reducing chemicals and oxygen-free equipment. TEM images of the as-synthesized MnBi@Bi particles with a rough surface are shown in **Figure 4A (ii),** while TEM images of Bi nanospheres with a smooth surface are shown in **Figure 4A (i)**. The TEM image of annealed MnBi is displayed in **Figure 4A (iii).** As shown in **Figure 4C (i),** no hysteresis is observed at 300 K. However, at 5 K, the particles do not reach saturation even at 50 kOe (=3.98×10^6 A/m)**, as shown in Figure 4C (ii).** This suggests that at room temperature, the MnBi@Bi particles exhibit a superparamagnetic behavior, characterized by the absence of hysteresis and saturation. For both 5 K and 300 K, the magnetization steadily increases with reaction time, ranging from 12 to 72 hours **(Figure 4C (iii)).** This trend could be attributed to the higher density of Mn deposition on the particle surface as the reaction time is extended. The elemental distribution of the MnBi@Bi sample was shown in **Figure 4B**, revealing that a higher concentration of Mn on surface while Bi is concentrated within the particle.

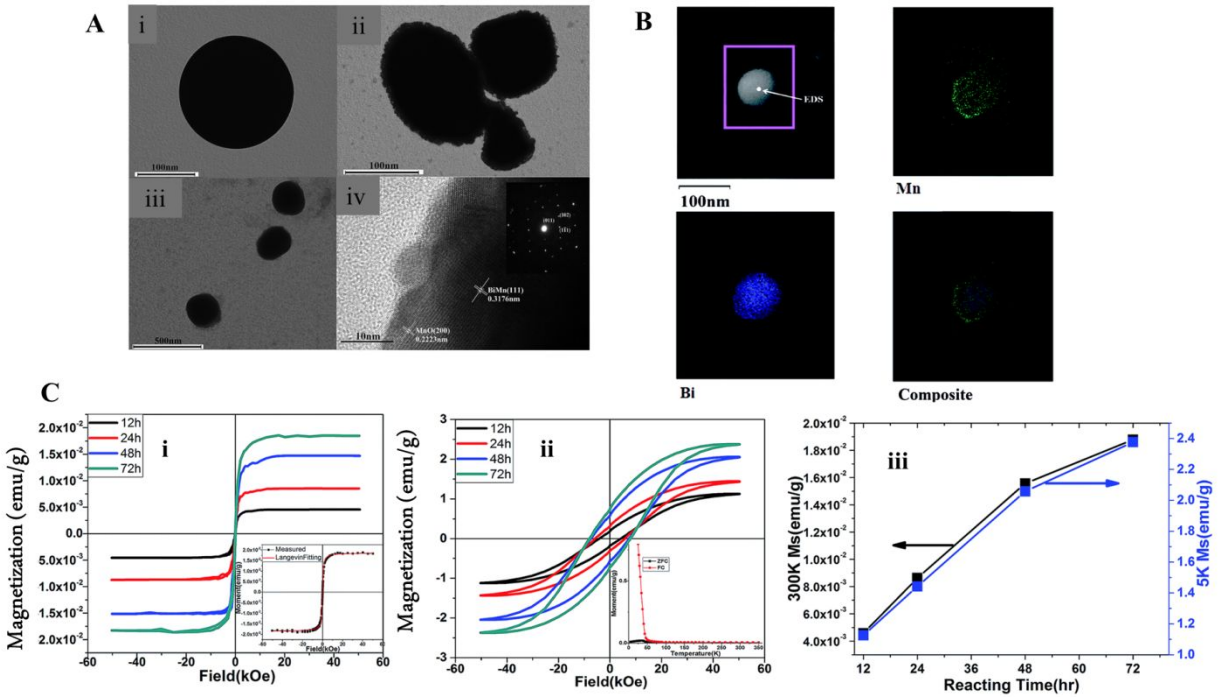

Figure 4. (A) (i) Initial Bi particles after rapid reduction, (ii) MnBi@Bi particles before annealing showing Mn around Bi particles, (iii) MnBi@Bi particles after annealing, (iv) MnO shell on the annealed MnBi@Bi particles. (B) elemental mapping results of annealed particles. (C) Magnetic hysteresis (M–H) loops of MnBi particles: (i) at 300 K (ii) at 5 K, and (iii) Ms as a function of reaction time from 12 h to 72 h.[105] Reproduced from ref. 105 with permission from RSC Publishing, copyright 2016.

2.2.4. Thermal decomposition

The thermal decomposition method involves the decomposition of metallic or organometallic precursors. While thermal decomposition allows for fast synthesis with controlled size, it poses safety risks due to the elevated temperatures which need to be carefully monitored.[97, 106] In Muzzi *et al.'s* study, they explored a low-temperature solvent-mediated thermal treatment as an effective post-processing method to reduce local internal stress and enhance the magnetic hardening of chemically synthesized particles. They reported nonstoichiometric cobalt ferrite particles with an average size of ~32 nm, produced through the thermal decomposition method (see **Figure 5A**). These particles were then subjected to solvent-mediated annealing at temperatures ranging from 150 to 320 °C in an inert atmosphere. As illustrated in **Figure 5B-C**, the dried cobalt ferrite nanoparticles ($Co_{0.4}Fe_{2.6}O_4$, abbreviated as CFO) exhibit reduced coercivity when annealed at 210 °C in an oven (labeled as CFO210-oven), compared to both nanoparticles annealed at the same temperature in a solvent (labeled as CFO210) and the untreated initial sample (labeled as CFO). This difference is primarily due to the varying surface-surfactant interactions in the two processes. This post-synthesis treatment resulted in a 50% increase in the coercive field without altering the remanence ratio or spontaneous magnetization. Consequently, the energy product and magnetic energy storage capacity—critical properties for applications such as permanent magnets and magnetic hyperthermia—were boosted by approximately 70%. They also found that the choice of the solvent where the mild annealing takes place plays a crucial role in controlling the final properties of the nanoparticles. In contrast, traditional annealing at higher temperatures (above 350°C) did not effectively release lattice stress, leading to a decrease in the

initial coercive field. The approach presented here offers a promising method for enhancing the magnetic properties of nanoparticles, making it particularly attractive for materials like cobalt ferrite, which are being studied for use in the development of rare-earth-free permanent magnets.[107]

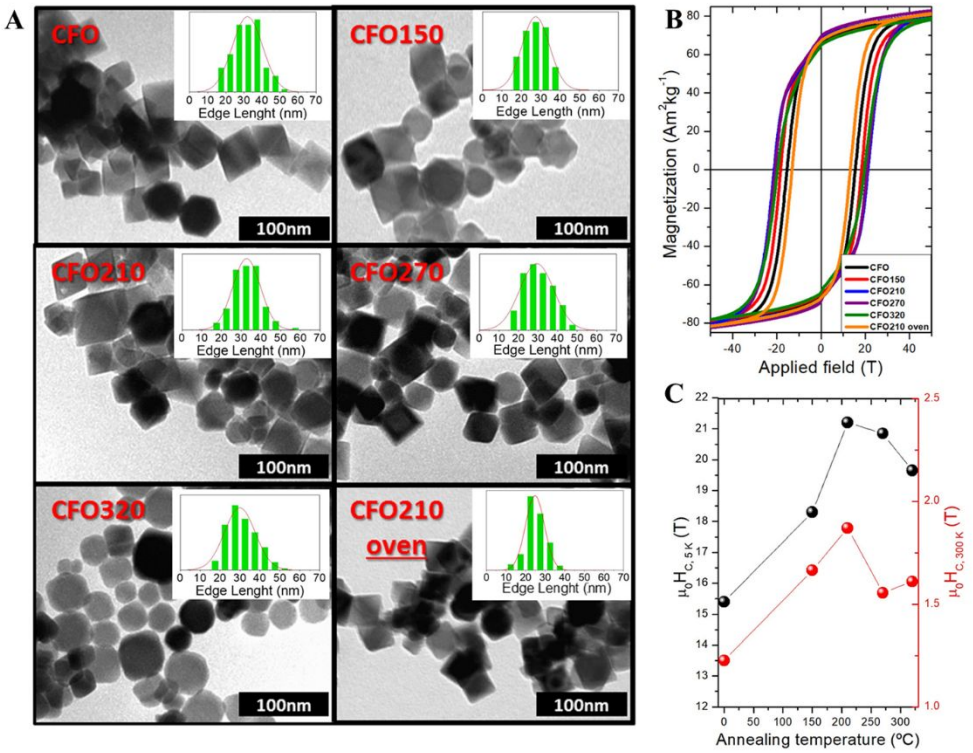

Figure 5. (A) TEM images and corresponding particle edge length histograms for as-prepared and annealed particles. (B) Hysteresis loops for the as-prepared and annealed cobalt ferrite particles measured at 5 K. (C) The coercive field (μ_0H_C) measured at 5 K (black) and 300 K (red) as a function of the annealing temperature. [107] Reproduced from ref. 107 with permission from American Chemical Society, copyright 2022.

2.2.5. Ball milling

It is generally known that ball milling procedures are versatile in producing metastable systems and thus, used in numerous study domains.[108-110] When analyzing data from ball-milled samples, it is crucial to consider their unique disordered nature. Magnetic properties are influenced by two key length scales: the nanometric scale of crystalline structures and the micron-sized powder particles. These scales collectively define the soft magnetic behavior in mechanically alloyed powders.[111] Grain size refinement in milling is controlled by the mechanochemical agitation, powder properties, and defects introduced during the processing and thermal recovery stages. Based on the mechanical energy applied to the sample inside the chamber, mechanochemical milling can be divided into two groups: low energy ball mills (LEBM) and high energy ball mills (HEBM).[112]

Attyabi *et al.* used two surfactant-assisted ball-milling methods to prepare $Mn_{52}Al_{45.7}C_{2.3}$ flakes with varying diameters, utilizing barrel and cylindrical containers (**Figure 6**).[113] The microstructure and magnetic properties varied depending on the shape of the container and the duration of ball milling (2, 5, and 10

hours). In cylindrical containers, the milled powders are micron-sized, flake-like particles with cracks, showing the dominance of impact forces (Figure 6A (i-iii)). Early milling stages cause compressive strain, forming flake shapes, while longer milling narrows grain size without altering the shape (Figure 6A (iii)). In contrast, powders milled in barrel containers have smaller grain sizes and porous, step-like surfaces (Figure 6B (iv-vi)), where nanoparticles aggregate, indicating the predominance of shear forces. Over time, these forces break the particles into Mn-Al-C nanoparticles. After extended milling (10 hours), shear and impact forces bond the nanoparticles, leading to particle necking (Figure 6B (vi)). Morphological analysis revealed that the powders milled in a barrel-shaped container exhibited a higher amount of τ-phase compared to those milled in a cylindrical container. According to the theory of plasticity, the shape of the barrel container promotes even stress distribution, resulting in controlled milling and better preservation of the τ-phase.[114, 115] The shape of the cylindrical container led to uneven stress distribution, causing irregular milling and more τ-phase decomposition, which diminished the material's magnetic quality. When comparing the powders milled using barrel containers to those milled with cylindrical containers, a significant increase in M_S and M_r was observed. The magnetic properties also showed dependency on ball milling time. The powders milled in barrel containers for two hours had the highest M_S of 52.49 emu/g (=52.49 A·m²/kg) and M_r of 24.10 emu/g (=24.10 A·m²/kg). Furthermore, the barrel containers produced a more uniform strain distribution and higher shear stress, leading to a stable τ-phase at a relatively low strain microstructure.

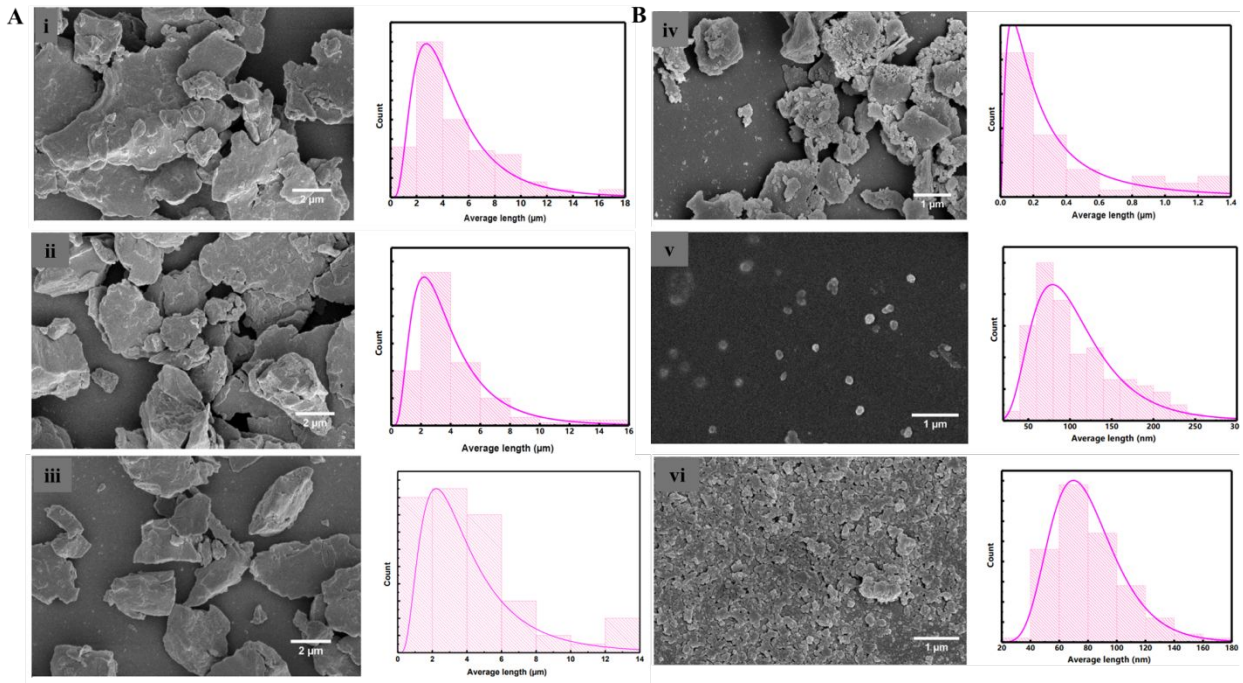

Figure 6. SEM images and particle size distribution of $Mn_{52}Al_{45.7}C_{2.3}$ milled during different times and using various containers: A: (i) 2 h, cylindrical container, (ii) 5 h, cylindrical container, (iii) 10 h, cylindrical container, B: (v) 2 h, barrel container, (vi) 5 h, barrel container, and (vii) 10 h, barrel container.[113] Reproduced from ref. 113 with permission from MDPI, copyright 2022.

2.2.6. Laser ablation

Laser synthesis of colloids is a physicochemical method to produce particles or nanoparticles. Using this technique, a target material submerged in a liquid (**Figure 7**) is laser-ablated to create a nanoparticle colloidal solution.[116] In a chamber with a continuous liquid flow, a thin wire that is supplied constantly can be employed as the ablation target in place of a bulk target. Advanced configurations for ablation include devices that provide remote control through the internet at any time. A solution containing micro- or nanometer-sized particles, or micro/nanomaterials may fragment or melt when exposed to a laser beam, producing a new colloidal solution**.** These laser-generated colloids, in some situations, have "bare" surfaces (surface adsorbates may be supplied to them exclusively by the solvent). Under certain conditions, the liquid compresses the expanding laser-induced plasma plume more than usual, resulting in metastable material phases. As these phases may have better qualities in parametric regions of interest than their stable counterparts do, these phases are preferred in various applications.[117] Jia *et al.* suggested a strategic road map based on the fundamental idea of twin-free particles or grains to achieve the best possible magnetic characteristics in $L1_0$-MnAl permanent magnets, where nanoparticles were synthesized using three distinct methods: laser ablation, plasma arc discharge, and calciothermic reduction.[118] Twin formation was efficiently suppressed during the $\varepsilon \rightarrow \tau$ phase transformation by nanocrystallization due to the energy balance between strain and twin boundary energies, and grain or particle sizes less than the twin-suppression critical size of about 300 nm could have a twin-free microstructure.

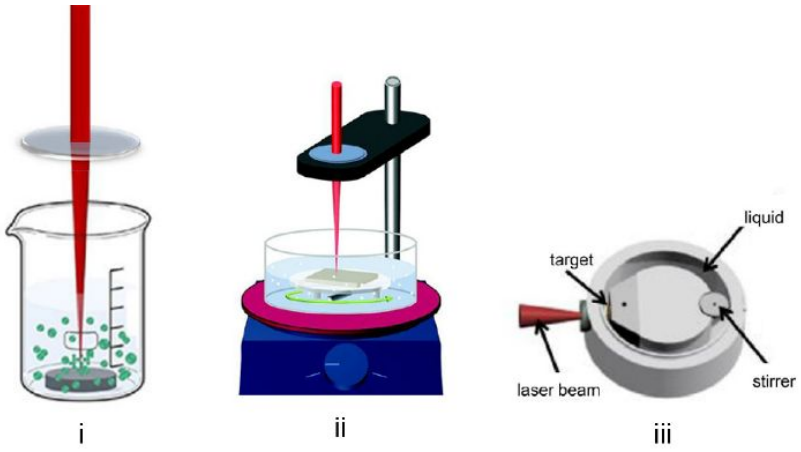

Figure 7. Basic setups for the laser synthesis of nanoparticles in liquids. Laser ablation of a bulk target material in a (i) steady liquid, (ii) magnetically stirred liquid and (iii) circulating liquid in a semi-batch flow cell.[116] Reproduced from ref. 116 with permission from American Chemical Society, copyright 2021.

3. Ink design and 3D printing

3.1. Ink design and formulation

Magnetic inks are composed of magnetic nanoparticles, dispersed in a mixture of solvents and stabilizers, often with additional performance-enhancing additives. Ink formulation is essential for additive manufacturing of high-performance devices in applications such as magnetic actuators,[119] magnetic sensors,[120] and customized magnets.[121, 122]

A critical aspect of formulating printable magnetic inks is choosing/selecting the right solvent to ensure the colloidal stability of the magnetic materials. The selected solvent not only has to be compatible with the material's surface ligands but also take into account viscosity, surface tension, and boiling point for effective dispersing and printing of nanoparticles.[123, 124] For example, the Hansen solubility parameter, or Hansen distance (Ra), can predict how well two molecules or compounds will dissolve in each other by quantifying the affinity between a solvent and a material based on their interactions, such as dispersion forces, dipolar interactions, and hydrogen bonds. The lower the value of Ra, the greater the compatibility between the solvent and the material, thus enhancing solubility. While Ra is not always available for magnetic materials, they can often be estimated using solvent's polarity. The right polarity, i.e., the compatible polarity of the solvent and materials helps estimate the aggregation tendency, which is critical for the ink to maintain its consistency without particle settling or nozzle clogging (**Figure 8A**). For example, for pristine oxide-based magnetic particles without surface ligands, the ink printability increases when solvent polarity increase (H_2O>EtOH>IPA>toluene>cyclohexane), as the electrostatic stabilization of surface oxide starts to play an increasingly important role. The volatility and boiling point of solvents are also important factors for a particular printing process. In the case of screen printing, less volatile solvents (e.g., terpineol) are desired to prevent potential clogging of the screen mesh, whereas more volatile solvents (e.g., isopropanol) are preferred in high-speed printing to facilitate rapid drying.[125-127] In some cases, mixed solvents are used to enhance the dispersion and rheological properties of inks by modifying the boiling point, surface tension, and solubility parameters.[128, 129]

While the magnetic nanoparticles in the magnetic inks are responsible for their unique functional properties, a key objective in their formulation is to integrate these nanoparticles into a stable colloidal dispersion to ensure their printability, so that the inks maintain their magnetic characteristics after the printing process. Colloidal stability refers to the ability of a colloidal system (a mixture where one substance is dispersed evenly throughout another) to resist aggregation or settling of the dispersed particles over time.[130] To achieve that, some functional polymers (polyvinyl pyridine, polyvinyl alcohol, ethyl cellulose, etc.) are used to modify the rheological properties of the ink (**Figure 8B**). The ink rheology, such as viscosity, describes its resistance to flow under applied shear; Thus, it directly influences ink behavior during printing. Different printing technologies require different viscosity levels. For example, inkjet printing demands inks with low viscosity, less than 40 mPa·s, to prevent nozzle clogging and facilitate smooth ejection, while extrusion-based printing can effectively handle inks with viscosities up to 10^4 Pa·s.[131] In the 3D printing of polymer-based inks, the ink flow behaviors, such as shear-thinning, have to be controlled. This ensures smooth extrusion of viscous inks through the nozzle and prevent overspreading upon deposition onto the substrate.[132-134] Thus, manipulating ink rheological properties is essential for developing advanced inks that perform reliably under various printing conditions, enhancing both the quality and efficiency of printed products.

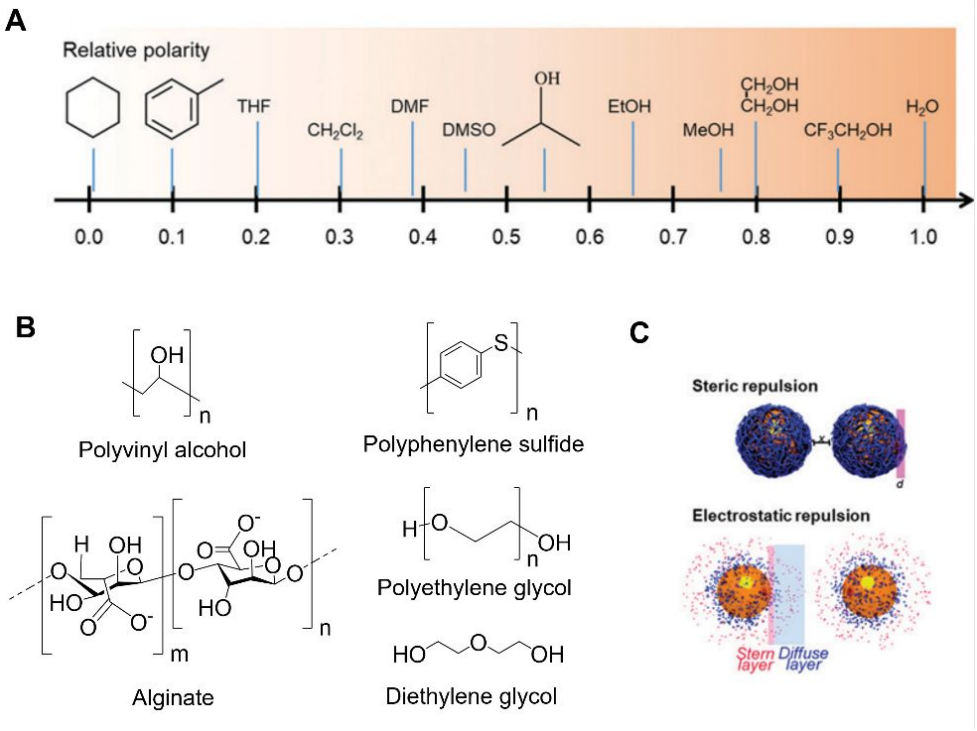

Figure 8. Solvent, surfactant, and binder chemistry for ink formulation. (A) Different types of solvents and their relative polarity to water.[135] Polarity influences dispersion forces, dipolar interactions, and hydrogen bonds, helping to estimate aggregation tendency. (B) Examples of some common binders and ink additives that modifies rheological properties, such as viscosity and storage moduli. (C) Schematic illustration of steric and electrostatic repulsion.[136] which helps to stabilize colloidal particles. Reproduced from ref. 135 with permission from Royal Society of Chemistry, copyright 2022. Reproduced from ref. 136 with permission from Royal Society of Chemistry, copyright 2015.

Another strategy for enhancing the colloidal stability of the inks is the use of surface ligands or surfactants. For polar solvents such as water, colloidal particles can be stabilized through electrostatic and/or steric interactions.[137-146] In nonpolar solvents, steric repulsion is vital for ink stability, and thus, surface ligands with solvophilic groups like long-chain alkyl groups are generally required.[15, 16] The DLVO theory (named after B. Derjaguin, L. Landau, E. Verwey, and T. Overbeek) explains how Van der Waals attractions and electrostatic repulsions from the counterion's double layer impact colloidal balance to make a stable suspension, highlighting the role of surfactants in enhancing colloidal stability and allowing higher concentration of ink material for applications (**Figure 8C**).[147, 148] Experimentally, electrostatic repulsion between particle double layers is semi-quantitatively evaluated by zeta potential, which can be controlled by the addition of surfactants. A high absolute value of zeta potential often suggests strong electrostatic repulsion among particles that prevents aggregation, whereas a low absolute value of zeta potential can lead to aggregation. However, additional thermal treatments or post-processing steps are often employed to remove the surfactant from the final product to ensure the optimum magnetic properties of the composite.[18, 149]

In addition, the volume fraction of the particles can be an important factor for the formulation of the magnetic ink. In particular, the magnetic particles are responsible for the magnetic properties of the ink, which are controlled by the amount of magnetic particles loaded in the suspension. Particle-particle

interactions can lead to a dramatic increase in viscosity at high particle loadings.[15, 150] For monodispersed particles, the relationship between ink viscosity and particle loading can be described by the Krieger and Dougherty model (**Eq. (1)**):[151, 152]

$$\eta_r = \left(1 - \frac{\varphi}{\varphi_m}\right)^{-b\varphi_m} \quad (1)$$

Here, φ denotes the particle volume fraction, which is proportion of the total suspension volume occupied by the dispersed particles. This parameter influences the viscosity, as higher φ values lead to increased particle interactions and resistance to flow. φ_m denotes the maximum packing fraction. For monodispersed spheres, the theoretical maximum packing fractions are 0.74 for a dense random packing, (while experimental values are 0.64 for dense random packings), and 0.6 for a loose random packing, respectively.[151, 153] b denotes a factor that accounts for the intrinsic viscosity of the particles and the specific interaction between particles in the suspension which is 2.5 for hard spheres. η_r denotes the relative viscosity, reporting the ratio of the dispersion fluid viscosity to that of the pure fluid.[154] It quantifies how the suspended particles modify the fluid's resistance to flow, with η_r increasing sharply as φ approaches the maximum packing fraction (e.g. $\eta_r \to \infty$ as $\varphi \to \varphi_m$).

Multiple solvents, additives, and magnetic materials (synthesized through a plethora of methods) have been combined and formulated as magnetic inks for additive manufacturing in recent years. Representative examples of these combinations and the applications of the additive manufactured materials are presented in **Table 2**.

Table 2. Examples of magnetic ink syntheses and formulations. DIW: direct ink writing; AJP: aerosol jet printing; IJP: inkjet printing; BJP: binder jet printing.

Magnetic material	Synthesis	Ink additives	Applications
$BaFe_{12}O_{19}/SrFe_{12}O_{19}$	High energy ball milling	Polyvinyl alcohol/polyethylene glycol /Solsperse 20000/water	DIW inks for magnetic separators[121]
Fe_3O_4	Co-precipitation	Alginate/CaCl2/methylcellulose/water	DIW inks for patterned hydrogel actuators[28]
Fe_2O_3	Commercial	Heptane	IJP inks for stretchable strain sensors[155]
$Ni_{0.5}Zn_{0.5}Fe_2O_4$	Commercial	N-methyl-2-pyrrolidone	AJP inks for microwave circuits[125]
$CoFe_2O_4$	Commercial	Ethanol/wax	Screen-printing ink for magneto-mechano-electric printed devices[2]

3.2. Printing methods

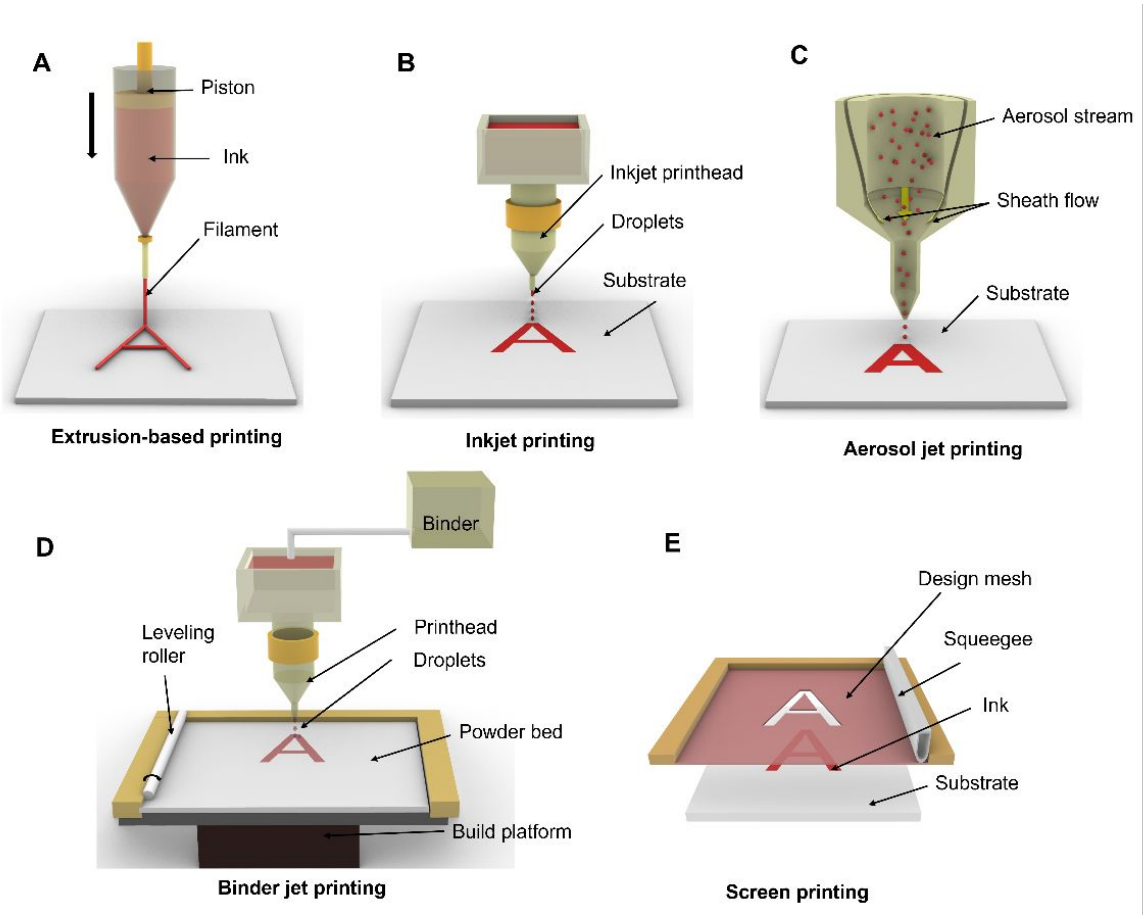

Figure 9. Schematics of ink-based printing techniques; (A) extrusion-based, (B) inkjet, (C) aerosol jet, (D) binder jet, and (E) screen printing.

The choice of printing method plays a crucial role in determining the resolution, scalability, and performance of magnetic devices. Among ink-based AM techniques, extrusion-based printing excels in handling high-viscosity inks and high particle loading, making it ideal for creating bulk magnetic structures.[156] In contrast, inkjet printing and aerosol jet printing are better suited for applications requiring high spatial resolution and precision, particularly for thin films and intricate patterns.[157-159] Binder jet printing is advantageous for fabricating large parts with diverse material options but often necessitates post-processing, such as sintering, to enhance magnetic properties.[160, 161] Lastly, screen printing is a robust and scalable method for depositing thick films, offering simplicity in design.[1, 162] The following sections provide an overview of each technique, including their working principles and post-printing treatments used to optimize magnetic performance.

3.2.1. Extrusion-based printing

Extrusion-based printing is a popular technique for the 2D and 3D printing of magnetic materials due to its affordability, simplicity, and versatility in material choices (**Figure 9A**). Extrusion printing uses external pressure either generated by a piston, pressurized air, or a screw force to extrude the ink through a nozzle to form structures with tailored magnetic properties. The printing resolution of these magnetic structures is typically controlled by the nozzle size. The main advantage of extrusion-based printing is the flexibility to

accommodate a wide range of materials, which not only can handle low viscosity dispersions but also high viscous inks with large particle loadings, opening the door to diverse magnetic material applications such as transformers,[163] magnets with complex shapes,[164] constant-flux inductors,[165] and electrochemical devices.[166] Thus, the viscoelastic properties of the ink are utilized to make self-supporting structures with or without a post printing treatment to fabricate functional magnetic materials.[5]

For extrusion-based printing, the Herschel-Bulkley model is normally used to describe the flow behavior of the ink (yield-stress ink is often used), where a minimum shear stress is required to induce the flow and the viscosity is shear rate-dependent **(Eq. (2)):**[133]

$$\tau = \tau_y + K\dot{\gamma}^n \quad (2)$$

Here, τ_y is the yield stress, $\dot{\gamma}$ is the shear rate, n is the shear thinning exponent and K is the viscosity parameter. However, this empirical model does not allow for the direct comparison of the different inks and consequently, alternative formulations of the Herschel-Bulkley model have been proposed based on more physically meaningful parameters.[167] For example, Hodaei *et al.* introduced a qualitative criterion to evaluate the printability of highly concentrated suspensions (magnetic inks) through a given nozzle using the yield point of the ink.[15] The yield point of a suspension is the cross point of loss and storage modulus. When the yield stress surpasses the maximum shear stress at the wall of the nozzle, it results in a plug flow where the flow behavior of the ink and its subsequent filament formation are hard to control.[168] Thus, the critical condition for suitable shear flow during DIW printing can be determined as (**Eq. (3)):**[15, 169]

$$\tau_{critical} = \left(\frac{\Delta P}{2L}\right).r \quad (3)$$

where, ΔP represents the maximum pressure drop in the system, r is the nozzle radius, and L is the nozzle length. The magnetic load of the ink increased close to the theoretical value by keeping the yield stress below the critical conditions for the successful printing of the formulation.

3.2.2. Inkjet printing

Inkjet printing (IJP) is an additive manufacturing technique for direct patterned deposition and involves ink being transferred from the reservoir to the nozzle head and ejected as microdroplets onto the substrate at controlled rates using mainly piezoelectric and thermal actuators (**Figure 9B**).[16, 17] Patterns are formed by moving either the substrate or the printhead, followed by the evaporation and solidification of the ink. Typically, the printed substrate undergoes post-processing, such as thermal annealing, sintering, or calcination to remove solvents, thus enhancing material adhesion and modifying the material structure.[170] Continuous and drop-on-demand (DOD) are the two main operational modes for this manufacturing technique, both offering high precision, small droplets, and flexible material choices for the formulation of the inks.

This technology relies on carefully formulated ink solutions with specific properties such as particle size, density, surface tension, and viscosity, to ensure stable droplet formation upon printing. Dispersed nanoparticles in the ink tend to form agglomerates, resulting in particle sedimentation and rapid solvent evaporation, which can cause nozzle clogging.[171] It is recommended to stabilize the ink with dispersing agents and use nanoparticle sizes no larger than 1/50th of the nozzle diameter.[172, 173] Although the ink viscosity (less than 40 mPa·s) and surface tension (10-50 $mN \cdot m^{-1}$) critically influence droplet formation and

size, the ink jetting performance also relies on the printing condition and nozzle size.[174, 175] The dimensionless inverse Ohnesorge number (Z) is used to estimate the jetting behavior of the ink (**Eq. (4)**):

$$Z = Oh^{-1} = \frac{\sqrt{\rho\gamma d}}{\eta} (4)$$

where, γ represents the surface tension, ρ is the density, η is the dynamic viscosity of the suspension, and d is the nozzle diameter. The inverse Ohnesorge number only considers the physical properties of the ink and characteristic printer length (d), making it practical and simple to use.[127, 176] However, there is a fair discrepancy in the literature about the ideal Z-value range, which indicates that the printability of the ink requires a comprehensive evaluation of peri and post printing factors.[127]

3.2.3. Aerosol jet printing

The aerosol jet printing (AJP) involves atomizing the ink into fine droplets and transporting them via a carrier gas through a nozzle to precisely deposit them on a substrate, where they are collimated by a sheath gas for focused and detailed layering (**Figure 9C**). This sheathing action (focusing) is crucial as it controls the droplet's trajectory towards the substrate, enhancing the precision of the deposition pattern (it can be as fine as 20 μm).[158] The formulation of the ink should have an optimal balance of viscosity and surface tension to maintain a good flow without spreading too widely upon contact with the substrate. Aerosol jet printing can handle up to 2500 mPa·s ink viscosities,[126] giving an additional advantage over inkjet printing which can only handle inks with viscosities of less than 40 mPa·s.

Similar to inkjet printing, the particle size and size distribution (in this case, it is aerosol) are critical for preventing nozzle clogging and ensuring stability, as too large particles can obstruct the nozzle, whereas very small ones may settle or not be carried efficiently by the aerosol stream. The commercial systems use ultrasonic atomization to create droplets by forming capillary waves on the ink surface. The produced droplet size is related to the ultrasound frequency, ink viscosity, and surface tension.[158, 177] Following atomization, the droplets are focused and directed to the substrate. The dimensionless Stokes number, St (**Eq. (5)),** can be used to describe the aerodynamic focusing of high-resolution printing, guiding the tuning of droplet size, nozzle diameter, and the flow rate as follows:[158]

$$St = \frac{\rho_p d_p^2 C_c}{18\mu} \frac{U}{D_n} (5)$$

where, ρ_p represents the droplet density, d_p is the droplet diameter, C_c is the slip correction factor, μ is the sheath gas viscosity, U is the average flow velocity, and D_n is the nozzle diameter. For standard thin-plate orifices, optimal focusing occurs for St values near 1,[178] whereas for weakly tapered nozzles used in the Nanojet systems, the St number is about 4.[179] In the context of aerosol jet printing, the Saffman force also becomes significant as it influences the droplets' motion within the aerodynamic focusing region of the deposition nozzle.[180] This force helps over-focus the droplets, especially larger ones, causing them to cross the centerline of the jet flow.[181] As a result, it contributes to a more concentrated deposition, aiding in the precise placement of the material on the substrate.[182] Overall, this technology has successfully served to manufacture materials for diverse applications that require a flexible and responsive attribute and permits high resolution and rapid patterning of magnetic materials, that can be of utility in multiple fields, such as microwave circuits,[125] soft robotics,[120] and biomedical engineering.[120, 183]

3.2.4. Binder jet printing

Binder jet printing (BJP) constructs parts layer by layer using a powder base material and a liquid binder (**Figure 9D**). Unlike IJP and AJP, the ink for binder jet printers does not contain particles, the magnetic nanomaterial comes from a powder bed. The binder acts as an adhesive that is selectively deposited onto the powder bed to form each layer of the object.[184] After printing, the object may be heated to debinding and then sintered or infiltrated to enhance its mechanical properties for final use. The characteristics of the binder ink, such as viscosity, curing time, and adhesion, are crucial because they directly influence how well the binder can be applied and set within the powder bed, affecting the precision of each layer and the structural integrity of the final part.[185-187] Similarly, process parameters like binder drop volume, printing speed, and drying time, need to be optimized as they control how deeply the binder penetrates the powder and how evenly it spreads, which are key factors in achieving the desired resolution.[188, 189] However, wettability and powder packing are two important factors that affect the choice of the binder, binder saturation, and the binder volume for an intended application.[190, 191] This technique is commonly employed for the printing of metal, ceramic, and metal matrix composites focusing on densification and microstructure evaluation of the final product.[18, 149, 192-194]

3.2.5. Screen printing

Screen printing is a printing technique where ink is pressed through a mesh or stencil onto a substrate, with certain areas blocked to prevent ink from passing through (**Figure 9E**). A blade or squeegee is dragged across the screen stencil, pushing ink into the mesh openings to transfer it onto the substrate during the squeegee stroke. When the screen rebounds away from the substrate, the ink remains on the substrate, forming the desired image or pattern. In screen printing, the deposited film has a rough texture due to the high viscosity of the ink. Using this technology, it is possible to get 100 μm thick features, widely used for printing flexible electronics and systems as inductors, resistors, capacitors.[195] Although this process is used for its simplicity, the patterning resolution depends on the ink rheology that has to be carefully designed to ensure high precision with fine edges without spreading beyond the pre-patterned area of the mask.[154]

Table 3. Examples of printed magnetic materials with associated post-printing treatments. Fe–6Si alloy: Fe-6.5 wt.% Si alloy.

Magnetic material	Fabrication	Ink formulation	Post-printing treatment	Magnetic properties
Fe_3O_4	Direct ink writing	Hydroxypropyl cellulose/ethylene glycol/water	Annealed at 180 ^{0}C, 10 min	M_S = 15.8 A·m²/kg[196]
Fe_3O_4	Aerosol jet printing	Toluene/terpineol	Each layer cured for 3 s with final post-curing of 60 s	Controllable magnetic response in the presence of an external magnetic field[197]
$Ni_{0.4}Zn_{0.6}Fe_2O_4$	Inkjet printing	Disperbyk-111/ dimethylformamide	Annealed at 700 °C, 10 min	M_S = 242 kA/m H_c = 4.751 kA/m [198]
Fe-6Si alloy	Binder jet printing	Commercial binders (ProMetal R-1, ExOne)	Annealed at 750 °C, 2 h	M_S = 1457 kA/m H_c = 31.83 A/m[193]
Ni-Mn-Ga alloy	Binder jet printing	Ethylene glycol monomethyl ether/ diethylene glycol	Sintered at 1070 °C, 2 h	M_S = 56.5 kA·m²/kg[194]
$BaFe_{12}O_{19}$	Screen printing	Di(propylene glycol) methyl ether/ epoxy	Cured at 120 °C, 10 min	M_S = 60 kA/m M_r = 20 kA/m H_C = 50 kA/m[199]

In addition to printing, it is worth mentioning that post-printing treatment is crucial for functional parts and devices. **Table 3** summarizes examples of post-printing treatments for magnetic devices fabricated using various printing methods. Formulated inks contain additives and binders to stabilize the dispersion and enhance its printability. However, most of these additives and binders are organic in nature and can negatively affect the magnetic properties of the final device by introducing non-magnetic barriers and thus, reducing its magnetic permeability.[200, 201] Some of the common post-printing treatments are sintering, annealing, and curing, where controlled temperatures ensure uniform distribution and alignment of magnetic nanoparticles in the system by reducing porosity and eliminating structural defects.[18, 194] For instance, Ni-Mn-Ga magnetic alloys fabricated using binder jet printing benefit significantly from post-printing sintering, offering the potential for magnetic field-induced strain due to controlled porosity. Mostafaei *et al.* showed how, as sintering temperatures rose from 1000 °C to 1100 °C, the Ni-Mn-Ga alloys relative densities increased from 45% to 99%. Increased relative density of a material, defined as the ratio of the actual density of the sintered material to the theoretical density of the fully dense material, expressed as a percentage, is important for evaluating the porosity and compactness of sintered materials which significantly affect their mechanical and physical properties. Below 1080 °C, solid-state sintering led to densities up to 80% with enhanced magnetic properties, while above 1090 °C, liquid phase sintering achieved ~99% density but reduced magnetization due to grain boundary segregation.[194] Wei *et al*. reported that an increase in the annealing temperature (from 1150 ^{0}C to 1350 ^{0}C) led to larger grain size and reduced porosity, which in turn decreased the hysteresis loss in ferrites.[202] To differentiate both post printing methods, it should be noted that annealing reduces material stress and improves ductility below the melting point, while sintering binds particles together near their melting point without fully melting them. Thus, post-printing annealing can be used to improve crystallinity and enhance magnetic properties by increasing grain size and reducing defects in the material.[193, 198] Along with controlling microstructure, another post-sintering technique is hot pressing, used to increase the densification and interfacial bonding between layers or particles within the composites.[1, 203] Ke *et al.* used hot pressing at 290 ^{0}C and 10 MPa to cure $Bi_{0.5}Sb_{1.5}Te_3$ (BST)/magnetic functional elements (MFEs)/epoxy films to ensure the compactness between thermoelectric and magnetic layers to enhance thermoelectric performance.[203] Also, hydrogel-based magnetic materials have been post-treated for Ca^{2+} crosslinking to form stable structures by immersing them in $CaCl_2$ solutions for 24 h.[28] In some cases, simple drying or thermal heating to remove the solvent is sufficient for the desired application.[15] Additionally, the controlled use of magnetic fields during post-printing treatments has been proven to enhance the alignment and orientation of the nanoparticles, leading to superior magnetic anisotropy and overall improved magnetic characteristics. More details about post-printing treatments can be found elsewhere.[12, 200, 204]

4. Device applications

4.1. Energy conversion

Thermoelectric (TE) devices offer great opportunities for the direct conversion of waste heat into electricity and solid-state refrigeration with no moving parts or environmental emission from refrigerants.[135, 205-207] TE devices generate electrical voltage from temperature differences across the material, based on the Seebeck effect. The addition of magnetic functional nanoparticles into TE materials to form thermoelectromagnetic (TEM) systems could enhance the TE conversion performance.[1, 208-211] **Figure 10(A-B)** show $Bi_{0.5}Sb_{1.5}Te_3$ (BST)/epoxy films with ordered dot magnetic arrays which were fabricated using screen printing and hot pressing to enhance TE conversion efficiency. The magnetic paste was printed in dot arrays on a polyimide substrate, followed by vacuum drying and printing of the TE paste, and then hot pressed at 573 K. Three

dot shapes (square, triangle, and hexagon) were tested, along with a continuous magnetic layer and a pristine TE film. The hexagonal-dot array film showed the best performance, with a room-temperature power factor of 1.51 $mWm^{-1}K^{-2}$, improving this value by 33.6% and 36.1% over the pristine and continuous layer films, respectively.[1] This superior performance was attributed to the alignment of the hexagonal dots with the hexagonal lattice structure of the BST composite, which enhanced the magnetic anisotropy and electrical conductivity.[212, 213] **Figure 10C** shows the power factor of screen printed samples. The maximum power factor of these films increased by 45% compared to reference sample.[203]

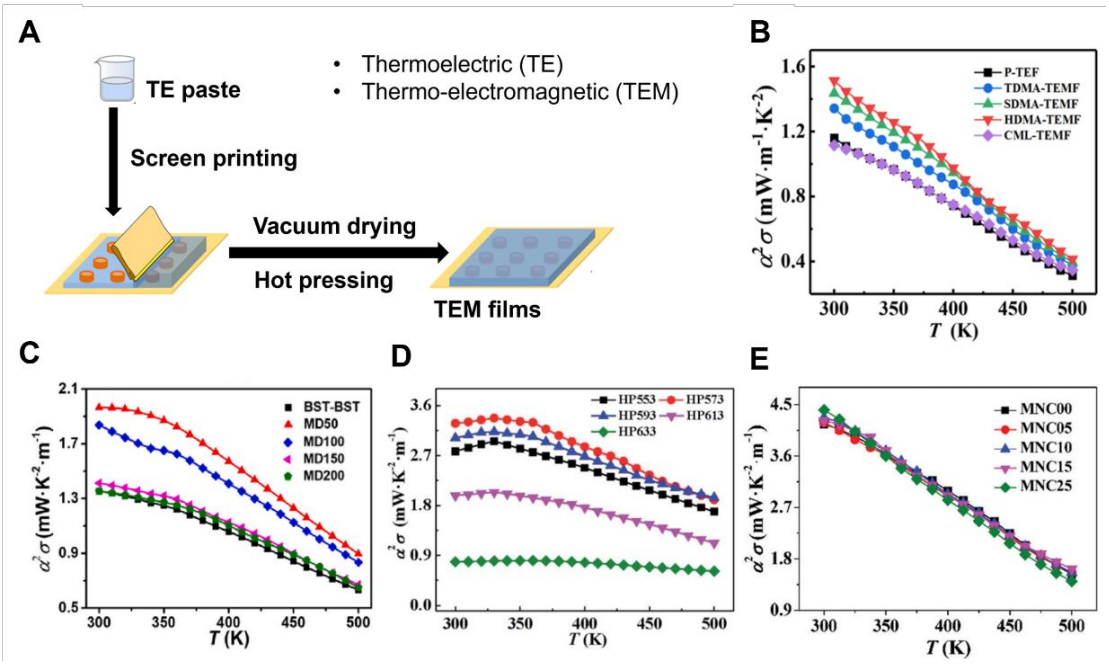

Figure 10. (A) Schematic illustration of the preparation of flexible Fe/BST/epoxy TEM films. (B) Temperature-dependent power factor of TE films and TEM films. The pristine BST/epoxy flexible TE film without a magnetic layer, labeled to as P-TEF. The single dots shaped as square, triangle, and hexagon, corresponding to dot magnetic arrays referred as SDMA, TDMA, and HDMA, respectively; the associated Fe/BST/epoxy flexible TEM films were labeled SDMA-TEMF, TDMA-TEMF, and HDMA-TEMF. A continuous Fe/epoxy layer and BST/epoxy layer, labeled as CML and CML–TEMF for the flexible TEM film.[1] (C) Power factor of BST/epoxy flexible films. The film without Fe-NPs referred to as BST-BST. Each sample, labeled MD50, MD100, MD150, and MD200, differs by the distance (ΔD) between magnetic functional elements (MFEs) in films.[203] (D) Power factor of 0.3%Ni/$Bi_2Te_{2.7}Se_{0.3}$ under the high pressure of 300 MPa. HP553, HP573, HP593, HP613, HP633 are 0.3%Ni/$Bi_2Te_{2.7}Se_{0.3}$ sintered at 553 K, 573 K, 593 K, 613 K and 633 K respectively, each under 300 MPa.[210] (E) Power factor of $Fe_3O_4/Bi_{0.5}Sb_{1.5}Te_3$ nanocomposites. A series of $xFe_3O_4/Bi_{0.5}Sb_{1.5}Te_3$ magnetic nanocomposites (x = 0, 0.05%, 0.10%, 0.15%, 0.25%) labeled to as MNC00, MNC05, MNC10, MNC15 and MNC25, respectively.[211] (A-B) Reproduced from ref. 1 with permission from American Chemical Society, copyright 2023. (C) Reproduced from ref. 203 with permission from Elsevier, copyright 2023. (D) Reproduced from ref. 210 with permission from Royal Society of Chemistry, copyright 2020. (E) Reproduced from ref. 211 with permission from Royal Society of Chemistry, copyright 2020.

In **Figure 10D,** a low temperature and high-pressure sintering approach has been recently adopted to develop Ni/$Bi_2Te_{2.7}Se_{0.3}$ nanocomposites by incorporating Ni nanoparticles into the n-type $Bi_2Te_{2.7}Se_{0.3}$ TE matrix.[214] Spark plasma sintered TE samples under various temperatures yielded a maximum power factor of 3.4 $mWm^{-1}K^{-2}$ for sintered Ni/$Bi_2Te_{2.7}Se_{0.3}$ nanocomposites at 573 K. The enhanced electrical conductivity due to the charge transfer from Ni nanoparticles along with increased Seebeck coefficient due to the electron multiple scattering and reduced thermal conductivity from phonon scattering resulted in a figure of merit (zT) of 1.1 at 360 K for sintered samples at 573 K.[210] Addition of REF magnetic nanoparticles to p-type TE materials has also shown significant enhancement of their TE performance. **Figure 10E** depicts the temperature dependent power factor of screen-printed films made by incorporating Fe_3O_4 nanoparticles into $Bi_{0.5}Sb_{1.5}Te_3$. The addition of 0.15 wt% Fe_3O_4 nanoparticles resulted in a 32% enhancement in zT compared to pure $Bi_{0.5}Sb_{1.5}Te_3$ due to the supermagnetic state of Fe_3O_4 nanoparticles leading to enhanced Seebeck coefficient and significantly reduced thermal conductivity from enhanced phono scattering.[211]

4.2. Sensing

Magnetic nanoparticles have attracted a growing interest in the development and fabrication of sensors.[2, 214-216] Up to now, a wide range of magnetic nanoparticle-based sensors and biosensors have been reported for detection of tumor cells,[217] nucleic acids,[218] proteins,[219-221] and vascular imaging.[222, 223] It is worth noting that different sensing applications may have different types of magnetic nanoparticle requirements.

Figure 11A shows a 3D printed flexible sensor using synthesized Fe_3O_4 at SiO_2 nanochains with low-friction surfaces and high durability for wearable applications. A DIW approach with dual nozzles was utilized to print the active magnetic component (i.e., Fe_3O_4 at SiO_2) and the encapsulating layer (i.e., PDMS) as passive packaging of the sensor. Improved mechanical properties of the polymer (polydimethylsiloxane, PDMS) were achieved by controlling the arrangement of the nanoparticles within the polymer through the application of magnetic fields. Furthermore, the addition of magnetic nanoparticles to PDMS as well as controlling their orientation led to an 8.4% increase in the average modulus of elasticity of the composite, compared to the pure PDMS sample. **Figure 11B** presents the comparison of the coefficient of friction for the printed sensor and the casted one. The optimized composite resulted in a reduction in the coefficient of friction by 27.7%, improving the wear resistance.[214]

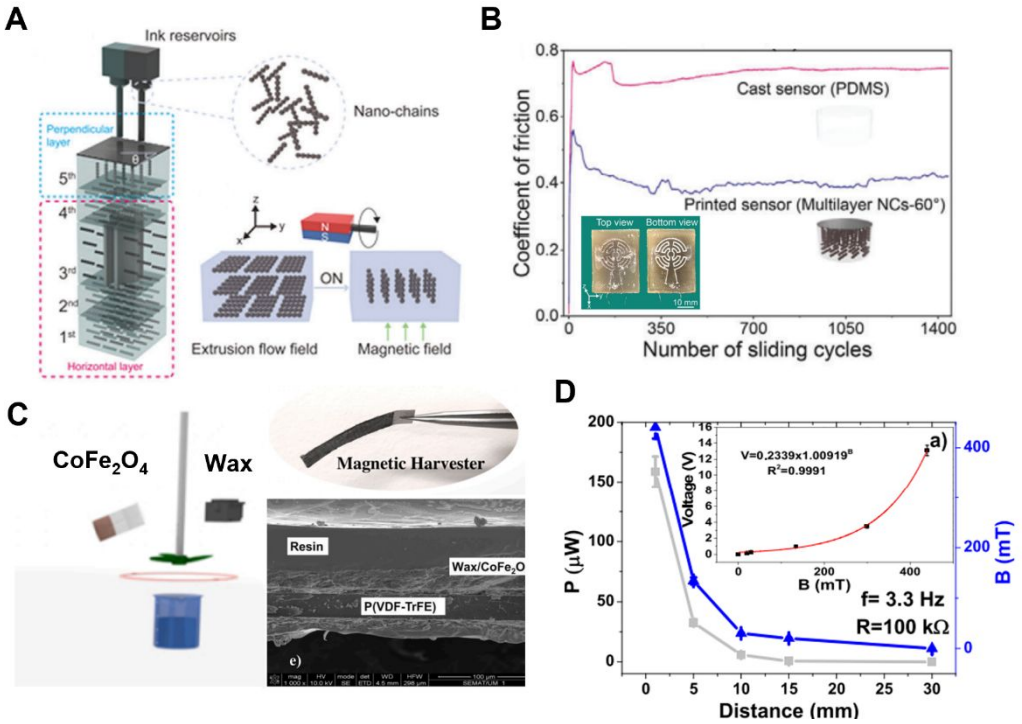

Figure 11. (A) Schematic illustration of magnetic fields orienting the Fe_3O_4 at SiO_2 nanochains in the extruded ink. (B) Coefficient of friction curves of sensors, with the inset showing optical images of the printed sensor.[214] (C) Schematic illustration of the preparation of piezoelectric/magnetic hybrid composites. (D) Harvested power, P, and magnetic field, B, as a function of the distance to the magnet.[2] (A-B) Reproduced from ref. 214 with permission from John Wiley and Sons, copyright 2024. (C-D) Reproduced from ref. 2 with permission from Elsevier, copyright 2022.

Furthermore, piezoelectric energy harvesting from magnetically coupled vibrational sources can be an effective way not only to harvest magnetic energy but also to promote magnetic sensing with self-power capabilities in the context of the Internet of Things and wearable applications. **Figure 11C** shows a screen-printed magnetic sensor/harvester comprised of a piezoelectric polymer (poly(vinylidene fluoride) with trifluoroethylene, P(VDF–TrFE)), $CoFe_2O_4$ nanoparticle/wax composite, silver electrodes, and a protective resin layer. The developed device exhibited mechano-magneto-electric energy conversion with an observed output power of almost 160 μW, a maximum power density of 9.7 $mWcm^{-3}$, and a sensitivity of 30 VT^{-1}, as shown in **Figure 11D**.[2]

The traditional manufacturing methods have limitations in creating complex 3D structures with integrated sensing functionalities. An *et al.* demonstrated an inductive force sensor for a robotic gripper fabricated using additive manufacturing technologies, featuring a NiZn-ferrite based magnetic core and a polymer-based helical spring **(Figure 12A).** The sensors showed excellent performance, with a sensitivity of 0.139 μH/N, high linearity (99.01%), minimal hysteresis, and robust endurance **(Figure 12B)**. The performance was validated with a robotic gripper employing the sensor and the force-sensing range could be adjusted with different spring designs. This approach enables the integration of sensors into compact spaces for electronic devices, benefiting future electronic systems like robotics.[224]

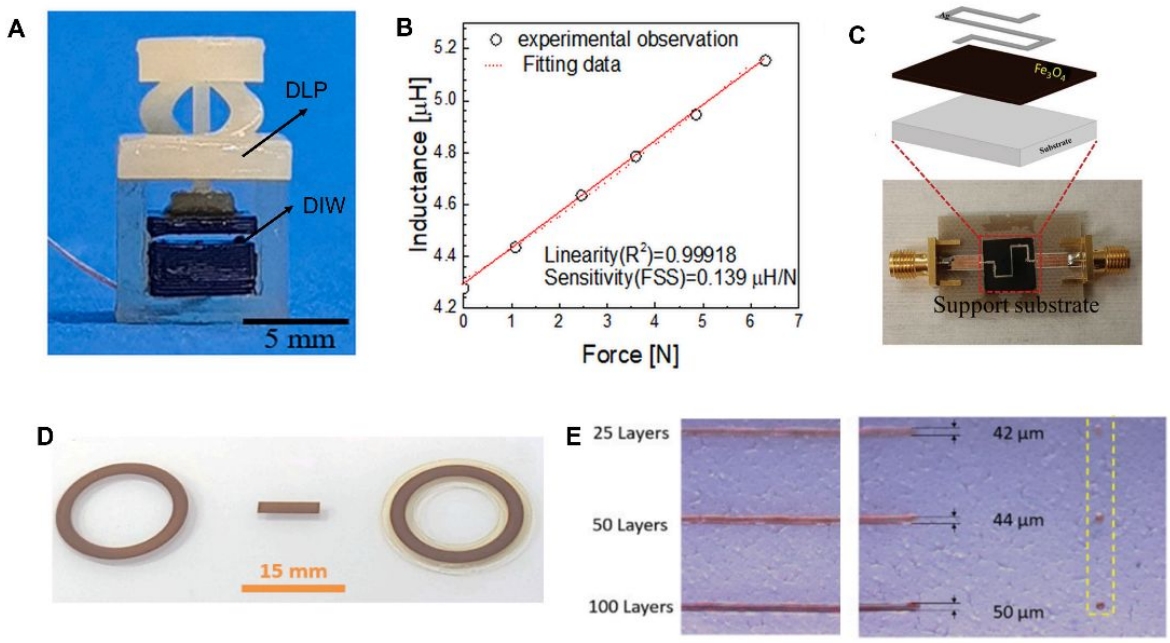

Figure 12. (A) Schematic illustration of an induction force sensor with a DIW printed NiZn-ferrite based magnetic core and a digital light processing (DLP) printed helical spring. (B) The force-sensing performance of the printed sensor and the inductance–force relation.[224] (C) Fully printed tunable inductor on magnetic Fe_3O_4 films.[225] (D) Ring-shaped inkjet-printed core (left) and inkjet-printed UV cured coating (right). The straight bar (in the middle) is a sample printed for magnetic measurements. (E) Printed lines and dots of the Mn-Zn ferrites on a polyethylene terephthalate substrate with various number of layers and measured width of the structures.[226] (A-B) Reproduced from ref. 224 with permission from Elsevier, copyright 2023. (C) Reproduced from ref. 225 with permission from Elsevier, copyright 2018. (D-E) Reproduced from ref. 226 with permission from Elsevier, copyright 2022.

Vaseem *et al.* demonstrated an inkjet-printed tunable inductor on top of printed magnetic Fe_3O_4 films **(Figure 12C**), showing the potential of magnetic inks in controllable radio-frequency applications. The inductor showed a saturation magnetization (M_S) of 1560 G and a magnetization frequency of 4.37 GHz.[225] Magnetization frequency refers to the rate at which the magnetization of a material is reversed or cycled, is a key parameter in applications involving alternating magnetic fields. Hrakova *et al.* reported a novel non-planar fluxgate sensor with an inkjet-printed core based on Mn-Zn ferrite nanoparticles **(Figure 12D)**. This sensor operated effectively within a linear range of ±1.5 mT, making it suitable for measuring electric currents, positions, and torque. With a printing pass of 100 layers **(Figure 12E)**, the sensor achieves a total thickness of 2.2 μm with a sensitivity of 10 mV/mT at an excitation frequency of 25 kHz.

5. Future perspectives

While significant advances and progress have been seen in recent years in formulating REF inks and 3D printing, challenges remain in terms of device performance and possible industrial-level manufacturing. For example, ink formulation and device optimization still heavily rely on the traditional experimental trial-and-error approach and several factors need to be carefully considered, including desired rheological properties, uniform particle distribution, optimized printing parameters, and maintaining magnetic properties post-printing.

During ink formulation, desired rheological properties are important to ensure that the ink flows smoothly through the nozzle and remains stable during printing. These properties depend on the selected ink-based printing method, as some tolerate high viscosity with dense particle loadings (e.g., screen printing) while others require less viscous inks (e.g., inkjet printing). Balancing magnetic particle loading is also critical, as it affects both the magnetic functionality and the printability of the ink, as overhigh loading may potentially cause clogging due to particle aggregation or material buildup within the nozzle.[227] While high particle loading is often necessary to achieve the desired magnetic performance, the development of novel ink formulation strategies, making use of new ink additives (e.g., optimizing surfactants and binders), is needed to reduce the risk of aggregation and clogging during printing.

For extrusion-based printing, several teams have proposed quantitative models to objectively describe shape fidelity using a systematic understanding of rheological properties and parameters.[228-231] The design of magnetic inks can benefit from learning knowledge of other printable ink systems, such as printable nanoparticles inks and even biological inks, as these ink models provide information on filament formation, extrusion uniformity, and filament fusion under gravity and surface tension. In addition, magnetic properties depend on particle loading and size,[18, 121, 232] yet there is no universal framework correlating different printing parameters such as line thickness, nozzle diameter, and extrusion pressure with particle loading and size. Therefore, future research is needed to develop quantitative models based on particle loading, rheology, and printing parameters to refine optimal printing conditions for magnetic applications.

Magnetic materials, both soft and hard, can undergo specific post-printing treatments that can alter their originally designed shapes. For soft magnetic applications, the matrix material (hydrogel or polymer) may swell or shrink, especially in "4D printing", where geometry changes over time in response to stimuli.[28] In some cases, sintering enhances the final magnetic properties by reducing defects, improving crystallinity, and aligning particles.[121, 233] Controlling the environmental conditions (e.g., sintering conditions and cooling rates) is essential to achieve desired microstructures, as grain size and boundary characteristics significantly affect magnetic properties like permeability and specific loss density.[18] Future research should focus on understanding the fundamental processing-properties relationship involving environmental conditions, microstructure, and magnetic properties.

Recent advances in data science have provided unique opportunities for the efficient optimization of REF magnetic materials and devices. While the conventional iterative approach is expert-dependent and time-consuming, recent advances in machine learning have the potential to rapidly optimize the ink properties, process parameters, and device performance. It also plays an increasingly important role in the design and discovery of new REF materials.[46, 234, 235] For example, a new Co_3Mn_2Ge-based REF magnet was recently reported by combining theories with experiments. The authors used high-throughput screening of the Inorganic Crystal Structure Database (ICSD) with density functional theory (DFT) calculations to predict key properties of materials and then trained machine learning models to predict order-disorder transitions, reducing the experimental burden by narrowing candidate lists to those with the highest likelihood of achieving desirable magnetic properties.[236] In our opinion, combining theoretical models with quantitative tests will be an important and powerful step toward the further implementation of high performance printed REF magnetic materials.

6. Acknowledgments

The authors thank the Texas Tech Startup Fund for the support. M. Z. acknowledges the support from the NSF (Grant No. CMMI-1400169 and DMR-2418915).

7. References

1. Y. Hu, X. Nie, S. Ke, W. Yan, X. Ai, W. Zhu, W. Zhao and Q. Zhang, *ACS Applied Materials & Interfaces*, 2023, **15**, 7112-7119.
2. R. Brito-Pereira, C. Ribeiro, N. Pereira, S. Lanceros-Mendez and P. Martins, *Nano Energy*, 2022, **94**, 106885.
3. Y. Li, Z. Li, Q. Wang, Z. Wu, C. Shi, S. Zhang, Y. Xu, X. Chen, A. Chen and C. Yan, *Additive Manufacturing*, 2023, **69**, 103542.
4. X. Zhang, Q. Wang, R. Zou, B. Song, C. Yan, Y. Shi and B. Su, *Engineering*, 2022, **15**, 196-205.
5. E. Peng, X. Wei, T. S. Herng, U. Garbe, D. Yu and J. Ding, *RSC advances*, 2017, **7**, 27128-27138.
6. M. Irfan, N. Dogan, A. Bingolbali and F. Aliew, *Journal of Magnetism and Magnetic Materials*, 2021, **537**, 168150.
7. J. Guzy, S. Chakravarty, F. J. Buchanan, H. Chen, J. M. Gaudet, J. M. Hix, C. L. Mallett and E. M. Shapiro, *ACS applied nano materials*, 2020, **3**, 3991-3999.
8. G. Song, M. Kenney, Y.-S. Chen, X. Zheng, Y. Deng, Z. Chen, S. X. Wang, S. S. Gambhir, H. Dai and J. Rao, *Nature biomedical engineering*, 2020, **4**, 325-334.
9. X. Du and T. E. Graedel, *Journal of Industrial Ecology*, 2011, **15**, 836-843.
10. E. Karal, M. A. Kucuker, B. Demirel, N. K. Copty and K. Kuchta, *Journal of cleaner production*, 2021, **288**, 125087.
11. J. Cui, M. Kramer, L. Zhou, F. Liu, A. Gabay, G. Hadjipanayis, B. Balasubramanian and D. Sellmyer, *Acta Materialia*, 2018, **158**, 118-137.
12. J. Cui, J. Ormerod, D. Parker, R. Ott, A. Palasyuk, S. Mccall, M. P. Paranthaman, M. S. Kesler, M. A. McGuire and I. C. Nlebedim, *Jom*, 2022, **74**, 1279-1295.
13. H. Wang, T. Lamichhane and M. Paranthaman, *Materials Today Physics*, 2022, **24**, 100675.
14. B. Qian, A. Shen, S. Huang, H. Shi, Q. Long, Y. Zhong, Z. Qi, X. He, Y. Zhang and W. Hai, *Advanced Science*, 2023, **10**, 2303033.
15. A. Hodaei, O. Akhlaghi, N. Khani, T. Aytas, D. Sezer, B. Tatli, Y. Z. Menceloglu, B. Koc and O. Akbulut, *ACS applied materials & interfaces*, 2018, **10**, 9873-9881.
16. E. Saleh, P. Woolliams, B. Clarke, A. Gregory, S. Greedy, C. Smartt, R. Wildman, I. Ashcroft, R. Hague and P. Dickens, *Additive Manufacturing*, 2017, **13**, 143-148.
17. Y. Kurokawa, K. Yamada and H. Yuasa, *Advanced Engineering Materials*, 2024, **26**, 2301069.
18. G. Kumari, T. Q. Pham, H. Suen, T. Rahman, P. Kwon, S. N. Foster and C. J. Boehlert, *Materials Chemistry and Physics*, 2023, **296**, 127181.
19. E. B. Joyee, A. Szmelter, D. Eddington and Y. Pan, *ACS Applied Materials & Interfaces*, 2020, **12**, 42357-42368.
20. S. Lantean, I. Roppolo, M. Sangermano, M. Hayoun, H. Dammak, G. Barrera, P. Tiberto, C. F. Pirri, L. Bodelot and G. Rizza, *Advanced Materials Technologies*, 2022, **7**, 2200288.
21. O. Dubinin, D. Chernodubov, Y. Kuzminova, D. Shaysultanov, I. Akhatov, N. Stepanov and S. Evlashin, *Journal of Materials Processing Technology*, 2022, **300**, 117393.
22. M. Ansari, E. Jabari and E. Toyserkani, *Journal of Materials Processing Technology*, 2021, **294**, 117117.

23. O. Tosoni, E. B. Mendonça, J. Reijonen, A. Antikainen, L. Schäfer, S. Riegg and O. Gutfleisch, *Additive Manufacturing*, 2023, **64**, 103426.
24. F. Bittner, J. Thielsch and W.-G. Drossel, *Progress in Additive Manufacturing*, 2020, **5**, 3-9.
25. H. Zhu, Y. He, Y. Wang, Y. Zhao and C. Jiang, *Advanced Intelligent Systems*, 2022, **4**, 2100137.
26. S. Wu, C. M. Hamel, Q. Ze, F. Yang, H. J. Qi and R. Zhao, *Advanced Intelligent Systems*, 2020, **2**, 2000060.
27. C. Ma, S. Wu, Q. Ze, X. Kuang, R. Zhang, H. J. Qi and R. Zhao, *ACS Applied Materials & Interfaces*, 2020, **13**, 12639-12648.
28. J. Simińska-Stanny, M. Nizioł, P. Szymczyk-Ziółkowska, M. Brożyna, A. Junka, A. Shavandi and D. Podstawczyk, *Additive Manufacturing*, 2022, **49**, 102506.
29. R. Bayaniahangar, S. B. Ahangar, Z. Zhang, B. P. Lee and J. M. Pearce, *Sensors and Actuators B: Chemical*, 2021, **326**, 128781.
30. R. Guan, H. Zheng, Q. Liu, K. Ou, D.-s. Li, J. Fan, Q. Fu and Y. Sun, *Composites Science and Technology*, 2022, **223**, 109409.
31. M. Y. Khalid, Z. U. Arif, A. Tariq, M. Hossain, K. A. Khan and R. Umer, *European Polymer Journal*, 2024, **205**, 112718.
32. S. Sundaram, M. Skouras, D. S. Kim, L. van den Heuvel and W. Matusik, *Science advances*, 2019, **5**, eaaw1160.
33. K. N. Al-Milaji, R. L. Hadimani, S. Gupta, V. K. Pecharsky and H. Zhao, *Scientific Reports*, 2019, **9**, 16261.
34. D. S. Kolchanov, V. Slabov, K. Keller, E. Sergeeva, M. V. Zhukov, A. S. Drozdov and A. V. Vinogradov, *Journal of Materials Chemistry C*, 2019, **7**, 6426-6432.
35. H. Song, J. Spencer, A. Jander, J. Nielsen, J. Stasiak, V. Kasperchik and P. Dhagat, *Journal of Applied Physics*, 2014, **115**.
36. P. Tiberto, G. Barrera, F. Celegato, M. Coïsson, A. Chiolerio, P. Martino, P. Pandolfi and P. Allia, *The European Physical Journal B*, 2013, **86**, 1-6.
37. O. Ergeneman, C. Peters, M. R. Gullo, L. Jacot-Descombes, S. Gervasoni, B. Özkale, P. Fatio, V. J. Cadarso, M. Mastrangeli and S. Pané, *Nanoscale*, 2014, **6**, 10495-10499.
38. L. Xie, C. Liang, Y. Qin, H. Zhou, Z. Yu, H. Chen, M. Z. Naeem, K. Qiao, Y. Wen, B. Zhang, G. Wang, X. Li, J. Liu, V. Franco, K. Chu, M. Yi and H. Zhang, *Advanced Functional Materials*, 2024, **n/a**, 2414441.
39. M. C. Maier, M. Leitner, C. O. Kappe and H. Gruber-Woelfler, *Reaction Chemistry & Engineering*, 2020, **5**, 1410-1420.
40. I. Galarreta-Rodriguez, A. Lopez-Ortega, E. Garayo, J. J. Beato-López, P. La Roca, V. Sanchez-Alarcos, V. Recarte, C. Gómez-Polo and J. I. Pérez-Landazábal, *Advanced Composites and Hybrid Materials*, 2023, **6**, 102.
41. F. Zhang, X. Miao, N. van Dijk, E. Brück and Y. Ren, *Advanced Energy Materials*, 2024, **14**, 2400369.
42. A. N. Surendran, R. Zhou and Y. Lin, *Journal of Medical Devices*, 2021, **15**, 024001.
43. S. Khashan, A. A. Odhah, M. Taha, A. Alazzam and M. Al-Fandi, *Scientific Reports*, 2024, **14**, 13293.
44. J. Mohapatra and J. P. Liu, *Handbook of magnetic materials*, 2018, **27**, 1-57.
45. K. Patel, J. Zhang and S. Ren, *Nanoscale*, 2018, **10**, 11701-11718.
46. A. Vishina, O. Eriksson and H. C. Herper, *Acta Materialia*, 2023, **261**, 119348.
47. D. Li, D. Pan, S. Li and Z. Zhang, *Science China Physics, Mechanics & Astronomy*, 2016, **59**, 1-17.
48. D. Li, Y. Li, D. Pan, Z. Zhang and C.-J. Choi, *Journal of Magnetism and Magnetic Materials*, 2019, **469**, 535-544.
49. K. P. Skokov and O. Gutfleisch, *Scripta Materialia*, 2018, **154**, 289-294.

50. F. Mazaleyrat, F. Calvayrac, Q. M. Ngo and N. Randrianantoandro, *Journal of Magnetism and Magnetic Materials*, 2022, **546**, 168892.
51. S. Ponomarova, V. Tatarenko, V. Odnosum, O. Ponomarov and Y. M. Koval, *Journal of Nanoparticle Research*, 2016, **18**, 1-11.
52. S. Goto, H. Kura, E. Watanabe, Y. Hayashi, H. Yanagihara, Y. Shimada, M. Mizuguchi, K. Takanashi and E. Kita, *Scientific reports*, 2017, **7**, 13216.
53. T. Keller and I. Baker, *Progress in Materials Science*, 2022, **124**, 100872.
54. K. K. Kefeni and B. B. Mamba, *Sustainable materials and technologies*, 2020, **23**, e00140.
55. S. A. Mathews and D. R. Babu, *Current Applied Physics*, 2021, **29**, 39-53.
56. P. Piekarz, D. Legut, E. Baldini, C. A. Belvin, T. Kołodziej, W. Tabiś, A. Kozłowski, Z. Kakol, Z. Tarnawski and J. Lorenzana, *Physical Review B*, 2021, **103**, 104303.
57. M. Hashim, A. Ahmed, S. A. Ali, S. E. Shirsath, M. M. Ismail, R. Kumar, S. Kumar, S. S. Meena and D. Ravinder, *Journal of Alloys and Compounds*, 2020, **834**, 155089.
58. O. K. Mmelesi, N. Masunga, A. Kuvarega, T. T. Nkambule, B. B. Mamba and K. K. Kefeni, *Materials Science in Semiconductor Processing*, 2021, **123**, 105523.
59. K. Shetty, L. Renuka, H. Nagaswarupa, H. Nagabhushana, K. Anantharaju, D. Rangappa, S. Prashantha and K. Ashwini, *Materials Today: Proceedings*, 2017, **4**, 11806-11815.
60. H. Zhao, Y. Dong, G. Wang, P. Jiang, J. Zhang, L. Wu and K. Li, *Chemical Engineering Journal*, 2013, **219**, 295-302.
61. S. J. Salih and W. M. Mahmood, *Heliyon*, 2023, **9**.
62. B. Rezaei, A. Kermanpur and S. Labbaf, *Journal of Magnetism and Magnetic Materials*, 2019, **481**, 16-24.
63. D. Lisjak and A. Mertelj, *Progress in Materials Science*, 2018, **95**, 286-328.
64. L. B. Kong, L. Liu, Z. Yang, S. Li, T. Zhang and C. Wang, in *Magnetic, ferroelectric, and multiferroic metal oxides*, Elsevier, 2018, pp. 287-311.
65. R. Jasrotia, J. Prakash, R. Verma, P. Thakur, A. Kandwal, F. Wan and A. Thakur, *Physica B: Condensed Matter*, 2023, 415202.
66. S. Lu, Y. Liu, Q. Yin, J. Chen, J. Li and J. Wu, *Journal of Magnetism and Magnetic Materials*, 2022, **564**, 170068.
67. Z. Mosleh, P. Kameli, A. Poorbaferani, M. Ranjbar and H. Salamati, *Journal of Magnetism and Magnetic Materials*, 2016, **397**, 101-107.
68. Y. Zou, J. Lin, W. Zhou, M. Yu, J. Deng, Z. Chen, G. Luo and D. Wang, *Journal of Alloys and Compounds*, 2022, **907**, 164516.
69. Z. Shao and S. Ren, *Nanoscale Advances*, 2020, **2**, 4341-4349.
70. S. Mandal, A. Panigrahi, A. Rath, M. Bönisch, P. Sengupta, M. Debata and S. Basu, *ACS omega*, 2023, **8**, 13690-13701.
71. G. Varvaro, P. Imperatori, S. Laureti, D. Peddis, F. Locardi, M. Ferretti, C. Cannas, M. S. Angotzi, N. Yaacoub and A. Capobianchi, *Scripta Materialia*, 2024, **238**, 115754.
72. T. Ochirkhuyag, D. Tuvshin, T. Tsevelmaa, S. Hong, K. Odbadrakh and D. Odkhuu, *Acta Materialia*, 2024, **268**, 119755.
73. J.-P. Wang, *Journal of Magnetism and Magnetic Materials*, 2020, **497**, 165962.
74. J. Wang, Y. Jiang, M. Mehedi, J. Liu, Y. Wu and B. Ma, 2018.
75. Y. Jiang, M. A. Mehedi, E. Fu, Y. Wang, L. F. Allard and J.-P. Wang, *Scientific reports*, 2016, **6**, 25436.
76. V. Ly, X. Wu, L. Smillie, T. Shoji, A. Kato, A. Manabe and K. Suzuki, *Journal of Alloys and Compounds*, 2014, **615**, S285-S290.
77. N. Singh, V. Mudgil, K. Anand, A. Srivastava, R. Kotnala and A. Dhar, *Journal of Alloys and Compounds*, 2015, **633**, 401-407.
78. L.-J. Zhu, S.-H. Nie and J.-H. Zhao, *Chinese Physics B*, 2013, **22**, 118505.
79. S. Ibrahim, A. Shamah, Y. Abbas, F. Hanna, L. Marei and A. Hannora, *Egypt J. Solids*, 2005, **28**, 315-323.

80. M. Choi, Y.-K. Hong, H. Won, C.-D. Yeo, N. M. Shah, B.-C. Choi, W. Lee, H. Choi-Yim, W. Lee and J.-U. Thiele, *Journal of Magnetism and Magnetic Materials*, 2024, **589**, 171513.
81. B. A. Jensen, W. Tang, X. Liu, A. I. Nolte, G. Ouyang, K. W. Dennis and J. Cui, *Acta Materialia*, 2019, **181**, 595-602.
82. P. Kharel, B. Lama, M. Flesche, Z. Mehlberg, B. Lamsal, S. Valloppilly, Y. Zhou, D. J. Sellmyer and T. R. Paudel, *Journal of Physics D: Applied Physics*, 2022, **55**, 265003.
83. A. M. Gabay, G. C. Hadjipanayis and J. Cui, *Journal of Magnetism and Magnetic Materials*, 2020, **495**, 165860.
84. D. Zhang, S. Cao, M. Yue, W. Liu, J. Zhang and Y. Qiang, *Journal of Applied Physics*, 2011, **109**.
85. T. Saito, R. Nishimura and D. Nishio-Hamane, *Journal of magnetism and magnetic materials*, 2014, **349**, 9-14.
86. R. Rejali, D. Ryan, Z. Altounian, C. Boyer, Q. Lu, M. Wang, H. Zhang and M. Yue, *AIP Advances*, 2016, **6**.
87. W. Zhang, P. Kharel, S. Valloppilly, R. Skomski and D. J. Sellmyer, *Journal of Applied Physics*, 2015, **117**.
88. S. Mizukami, T. Kubota, F. Wu, X. Zhang, T. Miyazaki, H. Naganuma, M. Oogane, A. Sakuma and Y. Ando, *Physical Review B—Condensed Matter and Materials Physics*, 2012, **85**, 014416.
89. H. Kurt, K. Rode, H. Tokuc, P. Stamenov, M. Venkatesan and J. Coey, *Applied Physics Letters*, 2012, **101**.
90. B. Dieny, V. S. Speriosu, S. S. Parkin, B. A. Gurney, D. R. Wilhoit and D. Mauri, *Physical Review B*, 1991, **43**, 1297.
91. L. Hao and W. Xiong, *Calphad*, 2020, **68**, 101722.
92. S. U. Rehman, Z. Ahmad, A. ul Haq and S. Akhtar, *Journal of Magnetism and Magnetic Materials*, 2017, **442**, 136-140.
93. S. U. Rehman, Q. Jiang, W. Lei, K. Liu, L. Zeng, M. Ghazanfar, T. Ahmad, R. Liu, S. Ma and Z. Zhong, *Physica B: Condensed Matter*, 2019, **552**, 136-141.
94. Z.-Y. Zhang, J.-B. Sun, J.-H. Feng, P.-G. Ji and Y. Zhang, *Journal of Alloys and Compounds*, 2023, **945**, 169334.
95. L. Zhou, M. K. Miller, P. Lu, L. Ke, R. Skomski, H. Dillon, Q. Xing, A. Palasyuk, M. McCartney and D. Smith, *Acta Materialia*, 2014, **74**, 224-233.
96. F. Jimenez-Villacorta and L. H. Lewis, *Advanced permanent magnetic materials*, One Central Press Manchester, UK, 2014.
97. A. Ali, T. Shah, R. Ullah, P. Zhou, M. Guo, M. Ovais, Z. Tan and Y. Rui, *Frontiers in chemistry*, 2021, **9**, 629054.
98. V. L. Kurichenko, D. Y. Karpenkov, A. Y. Karpenkov, M. B. Lyakhova and V. V. Khovaylo, *Journal of Magnetism and Magnetic Materials*, 2019, **470**, 33-37.
99. A. S. Patil, A. V. Patil, C. G. Dighavkar, V. A. Adole and U. J. Tupe, *Chemical Physics Letters*, 2022, **796**, 139555.
100. S. Majidi, F. Zeinali Sehrig, S. M. Farkhani, M. Soleymani Goloujeh and A. Akbarzadeh, *Artificial cells, nanomedicine, and biotechnology*, 2016, **44**, 722-734.
101. F. Wang and X. Liu, in *Comprehensive Nanoscience and Technology*, eds. D. L. Andrews, G. D. Scholes and G. P. Wiederrecht, Academic Press, Amsterdam, 2011, DOI: https://doi.org/10.1016/B978-0-12-374396-1.00146-X, pp. 607-635.
102. Y. Li, Q. Kuang, X. Men, S. Wang, D. Li, C. Choi and Z. Zhang, *Nanomaterials*, 2021, **11**, 890.
103. N. J. M. Sebri, A. F. A. Latip, R. Adnan and M. H. Hussin, in *Green Sustainable Process for Chemical and Environmental Engineering and Science*, Elsevier, 2022, pp. 23-42.

104. A. B. Djurisic, Y. Y. Xi, Y. F. Hsu and W. K. Chan, *Recent patents on nanotechnology*, 2007, **1**, 121-128.
105. J. Sun, C. Li, Q. Huang, G. Liu, G. Han, S. Yu and S. Kang, *RSC advances*, 2016, **6**, 100035-100039.
106. S. Gul, S. B. Khan, I. U. Rehman, M. A. Khan and M. Khan, *Frontiers in Materials*, 2019, **6**, 179.
107. B. Muzzi, E. Lottini, N. Yaacoub, D. Peddis, G. Bertoni, C. de Julián Fernández, C. Sangregorio and A. López-Ortega, *ACS Applied Nano Materials*, 2022, **5**, 14871-14881.
108. C. Suryanarayana, *Progress in materials science*, 2001, **46**, 1-184.
109. C. Suryanarayana and N. Al-Aqeeli, *Progress in Materials Science*, 2013, **58**, 383-502.
110. P. Baláž, M. Achimovičová, M. Baláž, P. Billik, Z. Cherkezova-Zheleva, J. M. Criado, F. Delogu, E. Dutková, E. Gaffet and F. J. Gotor, *Chemical Society Reviews*, 2013, **42**, 7571-7637.
111. J. Blázquez, J. Ipus, L. Moreno-Ramírez, J. Álvarez-Gómez, D. Sánchez-Jiménez, S. Lozano-Pérez, V. Franco and A. Conde, *Journal of Materials Science*, 2017, **52**, 11834-11850.
112. J. Joy, A. Krishnamoorthy, A. Tanna, V. Kamathe, R. Nagar and S. Srinivasan, *Applied Sciences*, 2022, **12**, 9312.
113. S. N. Attyabi, S. M. A. Radmanesh, S. A. Seyyed Ebrahimi, H. Dehghan, Z. Lalegani and B. Hamawandi, *Materials*, 2022, **15**, 7919.
114. W. F. Hosford, *Mechanical behavior of materials*, Cambridge university press, 2010.
115. G. E. Dieter and D. Bacon, *Mechanical metallurgy*, McGraw-hill New York, 1976.
116. N. G. Semaltianos and G. Karczewski, *ACS Applied Nano Materials*, 2021, **4**, 6407-6440.
117. S. Crivellaro, A. Guadagnini, D. M. Arboleda, D. Schinca and V. Amendola, *Review of Scientific Instruments*, 2019, **90**.
118. Y. Jia, Y. Wu, Y. Xu, R. Zheng, S. Zhao, K. P. Skokov, F. Maccari, A. Aubert, O. Gutfleisch and J. Wang, *Acta Materialia*, 2023, **245**, 118654.
119. C. Kakoyiannis, J. Sorocki, I. Piekarz and M. Geissler, *International Journal of Microwave and Wireless Technologies*, 2023, **15**, 1412-1423.
120. S. Taccola, T. da Veiga, J. H. Chandler, O. Cespedes, P. Valdastri and R. A. Harris, *Scientific Reports*, 2022, **12**, 17931.
121. X. Wei, Y. Liu, D. Zhao, X. Mao, W. Jiang and S. S. Ge, *Journal of Magnetism and Magnetic Materials*, 2020, **493**, 165664.
122. B. Podmiljšak, S. Kobe, T. Tomše, M. Bek, T. Kotnik, L. S. Perše, E. Žagar, B. Saje, K. Žužek and S. Šturm, *Journal of Magnetism and Magnetic Materials*, 2023, **586**, 171165.
123. J. N. Coleman, M. Lotya, A. O'Neill, S. D. Bergin, P. J. King, U. Khan, K. Young, A. Gaucher, S. De and R. J. Smith, *Science*, 2011, **331**, 568-571.
124. G. Cunningham, M. Lotya, C. S. Cucinotta, S. Sanvito, S. D. Bergin, R. Menzel, M. S. Shaffer and J. N. Coleman, *ACS nano*, 2012, **6**, 3468-3480.
125. M. T. Craton, J. D. Albrecht, P. Chahal and J. Papapolymerou, *IEEE Transactions on Components, Packaging and Manufacturing Technology*, 2021, **11**, 865-871.
126. C. Goth, S. Putzo and J. Franke, 2011.
127. S. F. Kamarudin, N. H. Abdul Aziz, H. W. Lee, M. Jaafar and S. Sulaiman, *Advanced Materials Technologies*, 2301875.
128. K. G. Zhou, N. N. Mao, H. X. Wang, Y. Peng and H. L. Zhang, *Angewandte Chemie International Edition*, 2011, **46**, 10839-10842.
129. M. Yi, Z. Shen, S. Ma and X. Zhang, *Journal of Nanoparticle Research*, 2012, **14**, 1-9.
130. R. Chhabra and M. Basavaraj, *Coulson and Richardson's Chemical Engineering (Sixth Edition)(Sixth Edition, pp. 693–737). Butterworth-Heinemann. https://doi. org/10.1016/B978-0-08-101098-3.00014-7*, 2019.
131. J. K. Placone and A. J. Engler, *Advanced healthcare materials*, 2018, **7**, 1701161.

132. A. Ribeiro, M. M. Blokzijl, R. Levato, C. W. Visser, M. Castilho, W. E. Hennink, T. Vermonden and J. Malda, *Biofabrication*, 2017, **10**, 014102.
133. J. E. Smay, J. Cesarano and J. A. Lewis, *Langmuir*, 2002, **18**, 5429-5437.
134. S. E. Critchley and D. J. Kelly, *Journal of 3D printing in medicine*, 2017, **1**, 269-290.
135. M. Zeng, D. Zavanelli, J. Chen, M. Saeidi-Javash, Y. Du, S. LeBlanc, G. J. Snyder and Y. Zhang, *Chemical Society Reviews*, 2022, **51**, 485-512.
136. T. L. Moore, L. Rodriguez-Lorenzo, V. Hirsch, S. Balog, D. Urban, C. Jud, B. Rothen-Rutishauser, M. Lattuada and A. Petri-Fink, *Chemical Society Reviews*, 2015, **44**, 6287-6305.
137. X. Li, Y. Qin, C. Liu, S. Jiang, L. Xiong and Q. Sun, *Food chemistry*, 2016, **199**, 356-363.
138. J. K. Lim, S. A. Majetich and R. D. Tilton, *Langmuir*, 2009, **25**, 13384-13393.
139. A. Ciesielski and P. Samorì, *Chemical Society Reviews*, 2014, **43**, 381-398.
140. M. Zeng, S. A. Shah, D. Huang, D. Parviz, Y.-H. Yu, X. Wang, M. J. Green and Z. Cheng, *ACS applied materials & interfaces*, 2017, **9**, 30797-30804.
141. X. Wang, M. Zeng, Y.-H. Yu, H. Wang, M. S. Mannan and Z. Cheng, *ACS applied materials & interfaces*, 2017, **9**, 7852-7858.
142. J. Luo, M. Zeng, B. Peng, Y. Tang, L. Zhang, P. Wang, L. He, D. Huang, L. Wang and X. Wang, *Angewandte Chemie International Edition*, 2018, **57**, 11752-11757.
143. Y.-H. Yu, Y.-P. Chen, M. Zeng and Z. Cheng, *Materials Letters*, 2016, **163**, 158-161.
144. P. Krishnan, A. Al-Rabbat, B. Zhang, D. Huang, L. Zhang, M. Zeng, M. S. Mannan and Z. Cheng, *Process Safety and Environmental Protection*, 2019, **123**, 48-58.
145. L. Zhang, Q. Lei, J. Luo, M. Zeng, L. Wang, D. Huang, X. Wang, S. Mannan, B. Peng and Z. Cheng, *Scientific reports*, 2019, **9**, 163.
146. R. Ma, M. Zeng, D. Huang, J. Wang, Z. Cheng and Q. Wang, *Journal of Colloid and Interface Science*, 2021, **601**, 106-113.
147. Z. Adamczyk and P. Weroński, *Advances in colloid and interface science*, 1999, **83**, 137-226.
148. B. W. Ninham, *Advances in colloid and interface science*, 1999, **83**, 1-17.
149. L. Li, A. Tirado, B. S. Conner, M. Chi, A. M. Elliott, O. Rios, H. Zhou and M. P. Paranthaman, *Journal of Magnetism and Magnetic Materials*, 2017, **438**, 163-167.
150. J. Gebauer, V. Mackert, S. Ognjanović and M. Winterer, *Journal of colloid and interface science*, 2018, **526**, 400-409.
151. D. B. Genovese, *Advances in colloid and interface science*, 2012, **171**, 1-16.
152. I. M. Krieger and T. J. Dougherty, *Trans. Soc. Rheol*, 1959, **3**, 137-152.
153. C. Servais, R. Jones and I. Roberts, *Journal of food engineering*, 2002, **51**, 201-208.
154. Y. Zhang, Y. Zhu, S. Zheng, L. Zhang, X. Shi, J. He, X. Chou and Z.-S. Wu, *Journal of energy chemistry*, 2021, **63**, 498-513.
155. G. Hassan, M. U. Khan, J. Bae and A. Shuja, *Scientific reports*, 2020, **10**, 18234.
156. M. A. S. R. Saadi, A. Maguire, N. T. Pottackal, M. S. H. Thakur, M. M. Ikram, A. J. Hart, P. M. Ajayan and M. M. Rahman, *Advanced Materials*, 2022, **34**, 2108855.
157. K. Zub, S. Hoeppener and U. S. Schubert, *Advanced Materials*, 2022, **34**, 2105015.
158. E. B. Secor, *Flexible and Printed Electronics*, 2018, **3**, 035002.
159. S. Taccola, H. Bakhshi, M. Sanchez Sifuentes, P. Lloyd, L. J. Tinsley, J. Macdonald, A. Bacchetti, O. Cespedes, J. H. Chandler, P. Valdastri, W. Meyer and R. A. Harris, *Advanced Materials Technologies*, 2024, **9**, 2400463.
160. M. Ziaee and N. B. Crane, *Additive Manufacturing*, 2019, **28**, 781-801.
161. A. Mostafaei, A. M. Elliott, J. E. Barnes, F. Li, W. Tan, C. L. Cramer, P. Nandwana and M. Chmielus, *Progress in Materials Science*, 2021, **119**, 100707.
162. Z. Herrasti, E. d. l. Serna, G. Ruiz-Vega and E. Baldrich, *Reviews in Analytical Chemistry*, 2016, **35**, 53-85.

163. L. M. Bollig, P. J. Hilpisch, G. S. Mowry and B. B. Nelson-Cheeseman, *Journal of Magnetism and Magnetic Materials*, 2017, **442**, 97-101.
164. C. Huber, C. Abert, F. Bruckner, M. Groenefeld, O. Muthsam, S. Schuschnigg, K. Sirak, R. Thanhoffer, I. Teliban and C. Vogler, *Applied Physics Letters*, 2016, **109**.
165. Y. Yan, L. Liu, C. Ding, L. Nguyen, J. Moss, Y. Mei and G.-Q. Lu, 2017.
166. A. J. Bandodkar, C. S. López, A. M. Vinu Mohan, L. Yin, R. Kumar and J. Wang, *Science advances*, 2016, **2**, e1601465.
167. A. Z. Nelson and R. H. Ewoldt, *Soft matter*, 2017, **13**, 7578-7594.
168. G. Siqueira, D. Kokkinis, R. Libanori, M. K. Hausmann, A. S. Gladman, A. Neels, P. Tingaut, T. Zimmermann, J. A. Lewis and A. R. Studart, *Advanced Functional Materials*, 2017, **27**, 1604619.
169. J. S. Reed, 1995.
170. K. Hon, L. Li and I. Hutchings, *CIRP annals*, 2008, **57**, 601-620.
171. M. Addamo, V. Augugliaro, A. Di Paola, E. Garcia-Lopez, V. Loddo, G. Marci, R. Molinari, L. Palmisano and M. Schiavello, *The Journal of Physical Chemistry B*, 2004, **108**, 3303-3310.
172. H. Maleki and V. Bertola, *ACS Applied Nano Materials*, 2019, **2**, 7237-7244.
173. P. Sundriyal and S. Bhattacharya, *ACS applied materials & interfaces*, 2017, **9**, 38507-38521.
174. H. Maleki and V. Bertola, *Catalysis Science & Technology*, 2020, **10**, 3140-3159.
175. N. V. Kamanina, *Features of Liquid Crystal Display Materials and Processes*, 2011.
176. S. Mueller, E. Llewellin and H. Mader, *Proceedings of the Royal Society A: Mathematical, Physical and Engineering Sciences*, 2010, **466**, 1201-1228.
177. C. Rodes, T. Smith, R. Crouse and G. Ramachandran, *Aerosol science and technology*, 1990, **13**, 220-229.
178. P. Liu, P. J. Ziemann, D. B. Kittelson and P. H. McMurry, *Aerosol Science and Technology*, 1995, **22**, 293-313.
179. J. F. De La Mora and P. Riesco-Chueca, *Journal of Fluid Mechanics*, 1988, **195**, 1-21.
180. I. Akhatov, J. Hoey, O. Swenson and D. Schulz, *Journal of aerosol science*, 2008, **39**, 691-709.
181. S. Binder, M. Glatthaar and E. Rädlein, *Aerosol Science and Technology*, 2014, **48**, 924-929.
182. J. Q. Feng and M. J. Renn, *Journal of Micro-and Nano-Manufacturing*, 2019, **7**, 011004.
183. N. Wilkinson, M. Smith, R. W. Kay and R. Harris, *The International Journal of Advanced Manufacturing Technology*, 2019, **105**, 4599-4619.
184. S. Bose, D. Ke, H. Sahasrabudhe and A. Bandyopadhyay, *Progress in materials science*, 2018, **93**, 45-111.
185. M. Lanzetta and E. Sachs, *Rapid Prototyping Journal*, 2003, **9**, 157-166.
186. A. M. Elliott, P. Nandwana, D. Siddel and B. Compton, 2016.
187. X. Lv, F. Ye, L. Cheng, S. Fan and Y. Liu, *Ceramics International*, 2019, **45**, 12609-12624.
188. K. Lu and W. T. Reynolds, *Powder technology*, 2008, **187**, 11-18.
189. N. D. Parab, J. E. Barnes, C. Zhao, R. W. Cunningham, K. Fezzaa, A. D. Rollett and T. Sun, *Scientific reports*, 2019, **9**, 2499.
190. S. Shrestha and G. Manogharan, *Jom*, 2017, **69**, 491-497.
191. M. Kafara, J. Kemnitzer, H.-H. Westermann and R. Steinhilper, *Procedia Manufacturing*, 2018, **21**, 638-646.
192. W. Du, X. Ren, C. Ma and Z. Pei, 2017.
193. C. L. Cramer, P. Nandwana, J. Yan, S. F. Evans, A. M. Elliott, C. Chinnasamy and M. P. Paranthaman, *Heliyon*, 2019, **5**.
194. A. Mostafaei, P. R. De Vecchis, E. L. Stevens and M. Chmielus, *Acta Materialia*, 2018, **154**, 355-364.

195. A. E. Ostfeld, I. Deckman, A. M. Gaikwad, C. M. Lochner and A. C. Arias, *Scientific reports*, 2015, **5**, 15959.
196. M. Wajahat, J. H. Kim, J. Ahn, S. Lee, J. Bae, J. Pyo and S. K. Seol, *Carbon*, 2020, **167**, 278-284.
197. S. Taccola, H. Bakhshi, M. Sanchez Sifuentes, P. Lloyd, L. J. Tinsley, J. Macdonald, A. Bacchetti, O. Cespedes, J. H. Chandler and P. Valdastri, *Advanced Materials Technologies*, 2024, 2400463.
198. M. Bissannagari and J. Kim, *Ceramics International*, 2015, **41**, 8023-8027.
199. C. S. Smith, K. Sondhi, S. C. Mills, J. S. Andrew, Z. H. Fan, T. Nishida and D. P. Arnold, *Journal of Materials Chemistry C*, 2020, **8**, 12133-12139.
200. D. Brown, B.-M. Ma and Z. Chen, *Journal of magnetism and magnetic materials*, 2002, **248**, 432-440.
201. H. Abdolmaleki, P. Kidmose and S. Agarwala, *Advanced Materials*, 2021, **33**, 2006792.
202. X. Wei, Y. Pan and Z. Chen, *Journal of the European Ceramic Society*, 2022, **42**, 1522-1529.
203. S. Ke, X. Nie, X. Ai, X. Li, W. Xu, K. Fu, T. Chen, C. Liu, W. Zhu and P. Wei, *Materials Today Physics*, 2023, **38**, 101234.
204. K. Takagi, Y. Hirayama, S. Okada, W. Yamaguchi and K. Ozaki, *Science and technology of advanced materials*, 2021, **22**, 150-159.
205. M. Saeidi-Javash, K. Wang, M. Zeng, T. Luo, A. W. Dowling and Y. Zhang, *Energy & Environmental Science*, 2022, **15**, 5093-5104.
206. W. Shang, M. Zeng, A. Tanvir, K. Wang, M. Saeidi-Javash, A. Dowling, T. Luo and Y. Zhang, *Advanced Materials*, 2023, **35**, 2212230.
207. T. Varghese, C. Dun, N. Kempf, M. Saeidi-Javash, C. Karthik, J. Richardson, C. Hollar, D. Estrada and Y. Zhang, *Advanced Functional Materials*, 2020, **30**, 1905796.
208. Y. Zhao, X. Nie, C. Sun, Y. Chen, S. Ke, C. Li, W. Zhu, X. Sang, W. Zhao and Q. Zhang, *ACS Applied Materials & Interfaces*, 2021, **13**, 58746-58753.
209. Y. Chen, X. Nie, C. Sun, S. Ke, W. Xu, Y. Zhao, W. Zhu, W. Zhao and Q. Zhang, *Advanced Functional Materials*, 2022, **32**, 2111373.
210. S. Ma, C. Li, P. Wei, W. Zhu, X. Nie, X. Sang, Q. Zhang and W. Zhao, *Journal of Materials Chemistry A*, 2020, **8**, 4816-4826.
211. C. Li, S. Ma, P. Wei, W. Zhu, X. Nie, X. Sang, Z. Sun, Q. Zhang and W. Zhao, *Energy & Environmental Science*, 2020, **13**, 535-544.
212. M. Johnson, P. Bloemen, F. Den Broeder and J. De Vries, *Reports on Progress in Physics*, 1996, **59**, 1409.
213. D. Sander, *Journal of Physics: Condensed Matter*, 2004, **16**, R603.
214. Z. Ma, Y. Wu, S. Lu, J. Li, J. Liu, X. Huang, X. Zhang, Y. Zhang, G. Dong and L. Qin, *Advanced Functional Materials*, 2024, 2406108.
215. Y. Xu and E. Wang, *Electrochimica Acta*, 2012, **84**, 62-73.
216. L. Gloag, M. Mehdipour, D. Chen, R. D. Tilley and J. J. Gooding, *Advanced Materials*, 2019, **31**, 1904385.
217. M. Poudineh, P. M. Aldridge, S. Ahmed, B. J. Green, L. Kermanshah, V. Nguyen, C. Tu, R. M. Mohamadi, R. K. Nam and A. Hansen, *Nature nanotechnology*, 2017, **12**, 274-281.
218. I. Willner, R. Baron and B. Willner, *Advanced Materials*, 2006, **18**, 1109-1120.
219. Y. Pan, X. Du, F. Zhao and B. Xu, *Chemical Society Reviews*, 2012, **41**, 2912-2942.
220. K. Chuah, Y. Wu, S. Vivekchand, K. Gaus, P. J. Reece, A. P. Micolich and J. J. Gooding, *Nature communications*, 2019, **10**, 2109.
221. D. M. Rissin, C. W. Kan, T. G. Campbell, S. C. Howes, D. R. Fournier, L. Song, T. Piech, P. P. Patel, L. Chang and A. J. Rivnak, *Nature biotechnology*, 2010, **28**, 595-599.
222. P. Ludewig, N. Gdaniec, J. Sedlacik, N. D. Forkert, P. Szwargulski, M. Graeser, G. Adam, M. G. Kaul, K. M. Krishnan and R. M. Ferguson, *ACS nano*, 2017, **11**, 10480-10488.

223. X. Y. Zhou, Z. W. Tay, P. Chandrasekharan, Y. Y. Elaine, D. W. Hensley, R. Orendorff, K. E. Jeffris, D. Mai, B. Zheng and P. W. Goodwill, *Current opinion in chemical biology*, 2018, **45**, 131-138.
224. T. An, S. Yoon and J. Kim, *Additive Manufacturing*, 2023, **71**, 103600.
225. M. Vaseem, F. A. Ghaffar, M. F. Farooqui and A. Shamim, *Advanced Materials Technologies*, 2018, **3**, 1700242.
226. D. Hrakova, P. Ripka, A. Laposa, D. Novotny, J. Kroutil, V. Povolný, O. Kaman and P. Veverka, *Journal of Magnetism and Magnetic Materials*, 2022, **563**, 170003.
227. F. Yang, X. Zhang, Z. Guo, S. Ye, Y. Sui and A. A. Volinsky, *Journal of Alloys and Compounds*, 2019, **779**, 900-907.
228. M. Di Giuseppe, N. Law, B. Webb, R. A. Macrae, L. J. Liew, T. B. Sercombe, R. J. Dilley and B. J. Doyle, *Journal of the mechanical behavior of biomedical materials*, 2018, **79**, 150-157.
229. L. Ouyang, R. Yao, Y. Zhao and W. Sun, *Biofabrication*, 2016, **8**, 035020.
230. B. Webb and B. J. Doyle, *Bioprinting*, 2017, **8**, 8-12.
231. H. Chen, Y. Liu, S. Balabani, R. Hirayama and J. Huang, *Research*, 2023, **6**, 0197.
232. E. M. Palmero, D. Casaleiz, J. de Vicente, B. Skårman, H. Vidarsson, P.-O. Larsson and A. Bollero, *Additive Manufacturing*, 2020, **33**, 101179.
233. R. Nazlan, I. Ismail, R. a. S. Azis, Z. Abbas, I. R. Ibrahim, F. M. Idris, F. N. Shafiee, A. S. Aripin and N. A. N. Busra, *Journal of Materials Science: Materials in Electronics*, 2018, **29**, 8688-8700.
234. A. Vishina, O. Eriksson and H. C. Herper, *Materials Research Letters*, 2023, **11**, 76-83.
235. H. Zhou, S. Yan, L. Wu, X. Wan and D. Wang, *Physical Review Materials*, 2023, **7**, 044405.
236. A. Vishina, D. Hedlund, V. Shtender, E. K. Delczeg-Czirjak, S. R. Larsen, O. Y. Vekilova, S. Huang, L. Vitos, P. Svedlindh and M. Sahlberg, *Acta Materialia*, 2021, **212**, 116913.

Data availability statements

No primary research results, software or code have been included and no new data were generated or analyzed as part of this review.